CNWRA *A center of excellence in earth sciences and engineering*

A Division of Southwest Research Institute™
6220 Culebra Road • San Antonio, Texas, U.S.A. 78228-5166
(210) 522-5160 • Fax (210) 522-5155

January 10, 2001

U.S. Nuclear Regulatory Commission
ATTN: Mrs. Deborah A. DeMarco
Office of Nuclear Materials Safety and Safeguards
Program Management, Policy Development, and Staff
Office of the Director
Mail Stop 8D-37
Washington, DC 20555

Subject: Transmittal of Journal Paper

Dear Mrs. DeMarco:

The purpose of this letter is to provide you a copy of a paper that will be submitted for publication in Nuclear Instruments & Methods in Physics Research, Section A. The research described in the attached paper, which is entitled, "Demonstration of a Collimated *In Situ* Method for Determining Depth Distributions Using Gamma-Ray Spectrometry" is derived from the Ph.D. work of Dr. Roland R. Benke. Because this work was not funded by the NRC you do not need to respond to this letter. However, if you have any questions regarding the content of the paper please contact me at (210) 522-5252 or Dr. Benke at (210) 522-5250.

Sincerely,

Budhi Sagar
Technical Director

GWW/cw
enlcosures

cc:					
	J. Linehan	K. Stablein	T. McCartin	W. Patrick	T. Nagy (SwRI Contracts)
	B. Meehan	S. Wastler	R. Codell	CNWRA Dirs	P. Maldonado
	E. Whitt	J. Firth	D. Esh	CNWRA EMs	
	J. Greeves		M. Rahimi	R. Benke	
	J. Holonich		B. Eid	J. Weldy	
	W. Reamer		C. McKenney	P. LaPlante	
	T. Essig			M. Smith	

Washington Office • Twinbrook Metro Plaza #210
12300 Twinbrook Parkway • Rockville, Maryland 20852-1606

DEMONSTRATION OF A COLLIMATED *IN SITU* METHOD FOR DETERMINING DEPTH DISTRIBUTIONS USING GAMMA-RAY SPECTROMETRY

Roland R. Benke*[†] and Kimberlee J. Kearfott[†]

* now at the Center for Nuclear Waste Regulatory Analyses, Southwest Research Institute, 6220 Culebra Road, San Antonio, TX, 78238-5166, USA

[†] University of Michigan, Department of Nuclear Engineering and Radiological Sciences, 2355 Bonisteel Boulevard, Ann Arbor, MI 48109-2104, USA

Abstract

In situ gamma-ray spectrometry uses a portable detector to quantify radionuclides in materials. The main shortcoming of *in situ* gamma-ray spectrometry has been its inability to determine radionuclide depth distributions. Novel collimator designs were paired with a commercial *in situ* gamma-ray spectrometry system to overcome this limitation for large area sources. Positioned with their axes normal to the material surface, the cylindrically symmetric collimators limited the detection of unattenuated gamma-rays from a selected range of polar angles (measured off the detector axis). By determining the depth distribution as a histogram, the collimation method presented in this paper represents an absolute method, while other *in situ* methods require *a priori* knowledge of the depth distribution shape. Other advantages over previous *in situ* methods are that this method does not require multiple gamma-ray emission energies, provides more detailed depth information, and offers a superior ability for characterizing complex depth distributions. Using a high-purity germanium spectrometry system,

collimated measurements of large area sources buried in attenuating materials demonstrated the method's ability to yield accurate depth information.

Keywords: Depth distribution; radionuclide characterization; *in situ*; gamma-ray spectrometry; nondestructive evaluation; collimation.

Introduction

In comparison to laboratory gamma-ray spectroscopy, *in situ* gamma-ray spectrometry characterizes a larger volume of material, requires less time to determine accurate radionuclide concentrations, and minimizes worker doses and the risk of radioactive contamination. The main limitation of *in situ* gamma-ray spectrometry lies in determining the depth distribution of radionuclides [1,2,3]. The *in situ* collimation method, presented in this paper, addresses this limitation.

Other *in situ* gamma-ray spectroscopic methods have been used to determine the depth distribution of radionuclides in soil [4-13]. However, these other methods require *a priori* assumptions of the depth distribution function. A more complete discussion of these methods can be found in an earlier paper related to this work [14]. The earlier paper presented an experimental calibration of the *in situ* method using a NaI(Tl) detector. In contrast, this paper focuses on applying the collimated *in situ* method to a Monte Carlo calibration of a high-purity germanium (HPGe) detector.

Recently, Monte Carlo codes have recently been used to calibrate *in situ* detectors [15-19]. The *In Situ* Object Counting System (ISOCS)[1] is a commercially available spectrometry system that bases its calibrations on Monte Carlo simulations of the measurement and source

geometry. The ISOCS calibration software calculates counting efficiencies for a variety of source geometries using the Monte Carlo N-Particle (MCNP)[2] transport code. The major benefit of the ISOCS calibration software is that it does not require costly and time-consuming experimental calibrations. Initially, the manufacturer performs a detailed characterization of the detector response using MCNP. The detector characterization is provided to the user and loaded into the ISOCS calibration software. Several source geometries are available, including boxes, cylinders, pipes, planes, spheres and Marinelli beakers. The ISOCS calibration software also has the capability of modeling collimators. A collimator template allows for the input of specific collimator dimensions. Once the materials, densities, source-to-detector distance, as well as the dimensions of sources, absorbers, and collimators have been input, the ISOCS calibration software calculates counting efficiencies for a desired range of gamma-ray energies. These efficiency data can be loaded into the counting software to obtain quantitative source activities directly from the photopeak count rates of a collected gamma-ray spectrum.

Theory

The system of equations describing the detector response from multiple sources is:

$$R_i = \sum_{j=1}^{n} \varepsilon_{i,j} \cdot s_j \qquad \text{for } i = 1 \,..\, m \qquad (1)$$

where R_i represents the photopeak count rate measured with the i^{th} collimator,

$\varepsilon_{i,j}$ represents the gamma-ray counting efficiency for the j^{th} source with the i^{th} collimator (i.e., the photopeak count rate for a unit gamma-ray emission rate from the source, unitless),

s_j represents the gamma-ray emission rate for the j^{th} source (equal to the source

activity multiplied by the gamma-ray yield),

n equals the number of sources, and

m equals the number of collimated measurements.

The counting efficiencies ($\varepsilon_{i,j}$) were computed from Monte Carlo simulations with the ISOCS calibration software.

For the reconstructions of the source activities, the solutions for the area source activities, equivalent to the s_j terms in Eq. (17) after a conversion from gamma-ray emission rate to activity, were determined by minimizing the following quantity:

$$\sum_{i=1}^{m}\sum_{k=1}^{p}\frac{\left(R_{i,k}^{fit}-R_{i,k}^{meas}\right)^2}{R_{i,k}^{meas}} \qquad (2)$$

where $R_{i,k}^{meas}$ represents the measured photopeak count rate, for the k^{th} gamma-ray energy with the i^{th} collimator, p equals the number of gamma-ray energies analyzed, and m equals the number of collimated measurements. $R_{i,k}^{fit}$ represents the fitted photopeak count rate, for the k^{th} gamma-ray energy with the i^{th} collimator and is described by the following relationship:

$$R_{i,k}^{fit}=\sum_{j=1}^{n}\left(\varepsilon_{i,j,k}\cdot Y_k\cdot a_j\right) \qquad (3)$$

where $\varepsilon_{i,j,k}$ represents the gamma-ray counting efficiency (unitless) for the k^{th} gamma-ray energy of the j^{th} source for the i^{th} collimator, Y_k represents the gamma-ray yield per decay (in units of γ s^{-1} Bq^{-1}) for the k^{th} gamma-ray, a_j represents the activity of the j^{th} source in units of Bq, and n equals the number of sources. A non-negativity activity constraint was applied to all of the reconstructions. Without normalizing the square of the count rate difference by the measured count rate, the solution would be skewed to better fit the measurements with the higher count

rates, because higher count rates imply larger magnitudes of the count rate differences and much larger squares of the count rate difference. For those analyses based on a single gamma-ray emission (i.e., p=1), the notation for the k^{th} gamma-ray and the summation over the gamma-ray emissions can be omitted in Eqs. (2) and (3).

ISOCS Monte Carlo Calibration

The physical dimensions of the collimators, presented in Fig. 1(a)-(d), were entered into the ISOCS calibration software. The materials, densities, source-to-detector distance, as well as the dimensions of sources, absorbers, and collimators were also input in the ISOCS calibration software and the counting efficiencies were calculated for a desired range of gamma-ray energies. For a particular measurement setup, these counting efficiencies were used to create a system of equations, described by Eq. (1), to relate the source activities with the measured photopeak count rate.

In this paper, "ISOCS" represents the entire spectrometry system[3], which consists of spectrometry equipment, calibration software, and counting software. All of the Monte Carlo calibrations were performed with the ISOCS calibration software. Therefore, the "ISOCS calibration software" directly implies the Monte Carlo calibration. All of the measurements were performed with the ISOCS-calibrated high-purity germanium detector. It should be noted that a complete ISOCS system can be purchased with simple, open-faced collimation consisting of lead annuli and an end piece (similar to the 0–34° collimator) that limits the field of view to polar angles between 0–15° or 0–45°. The purpose of the ISOCS collimation was to localize the field of view to a smaller area, which is advantageous for characterizations of a single object in areas with multiple sources (common to nuclear power plants, for example). However, the

simple, open-faced ISOCS collimation does not imply a separate *in situ* method for determining radionuclide depth distributions. The ISOCS spectrometry equipment was used with the collimators presented in Fig. 1(a)-(d) to determine radionuclide depth information.

For the reconstructions of the source activities, the ISOCS calibration software calculated the counting efficiencies for each combination of collimator and area source location. The physical dimensions of the collimators were entered into the ISOCS calibration software. Modeling of the 0–34° collimator was straightforward. However, the small flat edges (the small vertical dimension at the outer edge of the lower section for the 42–60° collimator shown in Fig. 2) could not be precisely modeled in the ISOCS calibration software. Therefore, the small flat edges of the 42–60°, 60–70°, and 70–80° collimators were simply extended at the same slope. For example, Fig. 2 depicts the extra material added to the edges of ISOCS model for the 42–60° collimator. The effect of the imprecise collimator modeling on the computed gamma-ray efficiencies is unknown, but was expected to be within the uncertainties of the computed efficiencies.

The ISOCS calibration software restricts the user to define collimators with openings at the detector face (i.e., shapes similar to the 0–34° collimator). Therefore, two efficiency calculations (referred to as "components") were required for the two-section collimators (42–60° for example): one for the upper section alone (0–60°) and one for the region *blocked* by the lower section (0–42°). Subtracting the efficiency for the region blocked by the lower section from the upper section's efficiency yielded the net efficiency for the two-section collimators. Based on the validation measurements[4] of several detectors and measurement geometries performed by the manufacturer[5], the 1σ uncertainties in the counting efficiencies calculated with ISOCS calibration software were estimated at 10.6% for gamma-ray energies of 50 – 100 keV,

7.5% for 100 – 400 keV, and 4.4% for 400 – 7000 keV. Based on a user manual[6] recommendation, a 6% uncertainty was assigned to the computed gamma-ray counting efficiencies for the 796 keV gamma-rays from the ^{134}Cs area sources.

The opening between the upper and lower collimator sections reduces as the polar angle increases (Fig. 1). As the collimator opening decreased in size for the larger polar angles, the efficiencies of the two components (the upper section alone and the region *blocked* by the lower section) of the net efficiency calculation approached one another in magnitude, and their difference (i.e., the net collimator efficiency) became small with respect to each component. Using the 70–80° collimator as an example, the efficiencies for the upper section alone (0–80°) and one for the region *blocked* by the lower section (0–70°) were close in magnitude. Therefore, 70–80° collimator's net efficiency became small with respect to the 0–70° and 0–80° efficiencies and on the order of the 6% uncertainty of the 0–70° and 0–80° efficiencies. In general for the 60–70° and 70–80° collimators, the magnitude of the net efficiency approached the uncertainty in each component's efficiency, which had an undesirable effect on the net collimator uncertainties. When the uncertainties were propagated for the net collimator efficiency, values exceeding 80% were obtained.

To overcome the problem of extremely large net efficiency uncertainties, the upper section of the 70–80° collimator in Fig. 1(d) was combined with the lower section of the 60–70° collimator in Fig. 1(c) to make a new 60–80° collimator with a larger opening. The 60–80° collimator was used in place of the 60–70° and 70–80° collimators for most of the ISOCS measurements, and in many cases, measurements were also acquired without a collimator (referred to as bare detector measurements) to replace the loss of a fourth collimated measurement.

The ISOCS calibration software divides the source into voxels and computes the gamma-ray efficiency for each voxel. Therefore, efficiency computations also account for gamma-rays emitted from regions of the source that were outside the collimator field of view and that encountered attenuation from the lead collimators. The ISOCS calibration software required the satisfaction of three convergence criteria for the computed counting efficiencies[6]. The three convergence criteria are:

(1) the percent difference of the integral counting efficiencies for 1024 voxels compared to 2048 voxels must be smaller in magnitude than the convergence value,

(2) the percent difference of the integral counting efficiencies for 2048 voxels compared to 4096 voxels must be smaller in magnitude than twice the convergence value, and

(3) the difference of criteria (1) and (2) must be smaller in magnitude than twice the convergence value.

While criterion (1) ensures that the desired percent convergence is attained, criteria (2) and (3) determine that the oscillations in the computed efficiencies are small.

All ISOCS efficiency calibrations were performed with a convergence value of 0.5% and a detector and collimator reference point numbers equal to four. The detector and collimator reference point numbers are related to the number of the pathways sampled from the source to the detector. Detector and collimator reference point numbers of four were found by the manufacturer[4] to be sufficient for most applications. At the expense of longer computation times, a lower convergence criterion of 0.1% and higher reference point numbers of six were also tested for a limited number of collimated geometries and compared to the actual source activities. However, changes in the computed efficiencies were less than 2% and well within the 6% uncertainty of computed efficiencies.

Collimator Measurement Geometries

Two collimator locations were chosen for measurements of the area sources. Measurements using the 0-34° collimator were taken at the center of the area sources and referred to as the full geometry shown in Fig. 3. The field of view of the collimators with larger values of the polar angle exceeded the dimension of the area sources in the full geometry. Therefore, all measurements (except for the 0-34° collimator measurements) of the buried area sources were taken normal to the area sources at the lower left corner and will be referred to as the ¼ geometry, shown in Fig. 4. Because the ¼ geometry limited the azimuthal region of interest from 0-360° to 0-90°, the photopeak count rates for the ¼ geometry should be multiplied by four to imply the photopeak count rates for a full geometry. The ¼ geometry had the effect of increasing the source area by a factor of four without requiring multiple measurements of the area source.

Results and Discussion

Detailed descriptions of the creation and characterization of the 102 cm by 102 cm area sources of ^{134}Cs are provided in an earlier paper [14]. The activities of the buried area sources were determined from the net collimator counting efficiencies for the 796 keV gamma-rays, calculated from the ISOCS calibration software. Analyses of multiple gamma-ray energies are presented in a later section. The densities of the absorber materials were 2.15 g cm^{-3} for concrete, 2.72 g cm^{-3} for aluminum, and 0.615 g cm^{-3} for wood (wood was modeled as cellulose in the ISOCS computations).

Activity Determinations of Two Area Sources at Different Depths

To demonstrate the ability of the ISOCS calibration software to adequately model the collimator and area sources in the experimental setups, two collimated measurements using ISOCS were acquired from a geometry with two buried area sources. Measurement geometries consisting of two area sources buried at different depths are referred to "two-source setups."

Measurements were performed using the 0–34° and 60–80° collimators for the two-source setup shown in Fig. 5. At the time of these measurements, the source activities were 128 ± 14 kBq (3.46 ± 0.38 μCi) for Source B and 522 ± 33 kBq (14.1 ± 0.9 μCi) for Source A. The activities reconstructed from the 0–34° and 60–80° measurements were 102 kBq (2.75 μCi) for Source B and 956 kBq (25.8 μCi) for Source A. Measurements taken with the 0–34° and 42–60° collimator yielded activities of 128 kBq (3.45 μCi) for Source B and 807 kBq (21.8 μCi) for Source A. Because the shallowest source was buried behind a significant amount of concrete (9.2 cm), it is not surprising that the 42–60° collimator with a "deeper" field of view resulted in a better prediction of the shallowest source activity than the 60–80° collimator. The counting times for these measurements ranged from 5.0 to 20 h with uncertainties due to counting statistics of 0.37 to 1.0%. It is important to keep in mind that the presented source geometry represented a very deep distribution where neither source was near the measurement surface. The consequence of a very deep source distribution is that longer counting times are required.

As in the activity reconstructions using the experimental calibrations [14], the small contributions from deeper sources were neglected in the collimated measurements of large polar angles that focused on the shallower sources. Due to the large attenuation by 18.4 cm of concrete, the counting efficiency for the deep source was found to significantly smaller than the shallow source for the 42–60° and 60–80° measurements. Therefore, the responses of the 42–60°

and 60–80° collimator measurements were made dependent only on the emission rate of the shallow source.

Another two-source setup was constructed by replacing the shallowest 9.2-cm layer of concrete with the 0.95-cm layer of aluminum. Measurements were collected using the 0–34° and 60–80° collimators, and the activities were reconstructed at 121 kBq (3.27 μCi) for Source B and 752 kBq (20.3 μCi) for Source A. As expected, the 60–80° collimator was better in determining the activity of shallowest source behind a thin absorber (0.95 cm of aluminum) than a thick absorber (9.2 cm of concrete). To assess the impact of an extra collimator measurement (three collimator measurements for two sources), the 42–60° measurement was included in the activity reconstructions and affected the activity determination for Source A at the deeper location. For this overdetermined situation, the extra measurement yielded an improvement by reconstructing an activity of 594 kBq (16.1 μCi) for Source A. For this shallower distribution, shorter counting times were required. Specifically, the counting times ranged from 2.67 to 5.00 h with uncertainties due to counting statistics of 0.25 to 0.5%.

Activity Determinations of Three Area Sources at Different Depths

Collimated measurements were also acquired from three buried area sources using the ISOCS spectrometry equipment. Setup I, shown in Fig. 6(a), was constructed and three measurements were taken: 0–34°, 60–80°, and a bare detector measurement. Counting efficiencies for each source and collimator were computed using the ISOCS calibration software and were combined with the measured photopeak count rates to create a system of three equations as described by Eq. (1). The source activities were determined from the solution of the system of three equations by minimizing Eq. (2) with a non-negative activity constraint.

Simplifications to the system of three equations (by neglecting the small contributions from the significantly attenuated deeper sources to the larger polar-angle measurements) were made to improve stability and reconstruction process and were similar to those made for the activity reconstructions using the experimental calibration [14]. For the 60–80° measurement, the counting efficiencies of the middle and deepest sources were a factor of 30 and 290 times smaller than for the shallowest source and were neglected (i.e., the detector response with 60–80° collimator became solely dependent on the emission rate of the shallowest source). For the bare detector measurement, the deepest source activity was a factor of 64 times smaller than the shallowest source and was neglected (i.e., the bare detector response became dependent on the emission rates from the shallowest and middle sources). The results for Setup I using the ISOCS system are presented in Table 1(a) and Fig. 7(a). Although the contributions of deeper sources can be neglected for some of the measurements, the shallowest source still has a significant impact on the smaller polar angle measurements used to characterize the deeper sources. Therefore, small underestimations of the shallowest source can result in greater overestimations of the deeper sources and can partially account for the 56% overestimation of the deepest source in Setup I.

Measurements using the 0–34°, 42–60°, 60–80° collimators were also acquired using Setup II, displayed in Fig. 6(b), and the activities reconstructions are shown in Table 1(b) and Fig. 7(b). For the 60–80° measurement, the counting efficiencies of the middle and deepest sources were a factor of 20 and 32 times smaller than those for the shallowest source and were neglected. For the 42–60° measurement, the deepest source's counting efficiency was a factor of 21 times smaller than the shallowest source and was neglected. Setup II is the shallow source setup, where all three sources are positioned behind materials that correspond to attenuation from

only 13 cm of soil. Although the shallowest source activity was determined within the source's 2σ activity uncertainty, the other two sources under the 6.7-cm layer of concrete were not resolved (i.e., were assigned a zero activity). To assess the impact of obtaining an additional measurement (four measurements for three sources), a bare detector measurement was combined with the three collimated measurements for a new activity reconstruction of Setup II with the results presented in Table 1(b). The additional measurement identified the presence of the deepest source, but underestimated its activity by factor of 5.5. In comparison to the counting statistics, the expected count rate from the weakest source was 6.5, 2.6, and 2.2 times higher than the 1σ counting statistics for the 0-34°, 42-60°, and bare detector measurements, respectively. In comparison to the background contributions in the net photopeak at 796 keV, the expected count rates solely due to Source C were roughly 12 and 6.3 times higher than the background count rates for the 42-60° collimator and bare detector measurements, respectively.

For Setup II, the fact that the strongest source was buried beneath only 0.95 cm of aluminum while the other sources were buried beneath the thickest absorber layer, 6.7 cm of concrete, made it difficult to identify the presence of the weak sources at greater depths. Slight modifications were made to Setup II to reduce the dominance of the shallowest source and to create Setup III. The locations of the 0.95-cm and 1.27-cm aluminum layers were switched and the 1.9-cm wood layer was moved from above Source C to directly above Source B. Fig. 6(c) displays Setup III. Again, measurements were taken with the 0–34°, 42–60°, 60–80° collimators. The source activities for Setup III were reconstructed following the same process for Setup II and the results are shown in Table 1(c) and Fig. 7(c). In this case, only the three collimated measurements were sufficient to identify and accurately determine the activity of the deepest source. However with a larger amount of attenuating material above the weaker sources and with

only 0.95 cm of aluminum and 1.9 cm of wood separating Source C and Source B, the weakest Source C was still not resolved (i.e., was assigned a zero activity). In comparison to the counting statistics, the expected count rate from the weakest source was 7.0 and 3.0 times higher than the 1σ counting statistics for the 0-34° and 42-60° collimator measurements, respectively. In comparison to the background contributions in the net photopeak, the expected count rate solely due to Source C was roughly 13 times higher than the background count rate for the 42-60° collimator measurement.

Setup IV, displayed in Fig. 6(d), was also constructed and measured with the ISOCS system. Based on four measurements (0–34°, 42–60°, 60–80°, and the bare detector) the activities were reconstructed and are presented in Table 1(d) and Fig. 7(d). For this shallow source setup, the four measurements not only identified the presence of each source, but also accurately determined the source activities. The shallowest source activity was precisely determined within 1% of the actual activity, while the middle and deepest sources were overestimated by 26% and 29%, respectively. Shown in Table 1(d) and Fig. 7(d), omitting the 42–60° collimator measurement and determining the activities from three measurements instead of four resulted in a 340% overestimation in the middle source's activity and a 29% underestimation in the deepest source's activity.

Analyses using Multiple Gamma-Ray Emissions

Thus far, all measurements and reconstructions of the area source activities were based on the 796 keV gamma-ray emission of ^{134}Cs with a yield of 85.4%. To demonstrate the ability of the collimated method to determine depth information from other gamma-ray energies, analyses were also preformed using lower and higher gamma-ray emissions from ^{134}Cs. The 475

keV emission, with a yield of 1.46%, was used as the low energy gamma-ray, and the 1365 keV emission, with a yield of 3.04%, was used as the high energy gamma-ray. For the multiple gamma-ray analysis, the ISOCS calibration software computed the counting efficiencies for the three gamma-ray emissions. The gamma-ray energies and yields were entered into the ISOCS calibration software, and the changes in the detection efficiencies for the different gamma-ray energies were automatically accounted for in the counting efficiency computations.

Using the same reconstruction procedure presented in the previous section, activity determinations for the three sources in Setup I, shown in Fig. 6(a), were performed for the multiple gamma-ray energies and are presented in Table 2. The measured data from each gamma-ray energy were also coupled to create a "combination reconstruction" of the area source activities in Table 2. The shallowest source's activity was determined solely from the 60-80° collimator measurements, and the other collimator measurements determining the activities of the deeper sources. For the combination reconstruction, the solutions for the area source activities were governed by Eqs. (2) and (3).

Because the 475 keV gamma-rays of the deepest source (beneath 18.4 cm of concrete, 1.0 cm of aluminum, and 2.2 cm of wood) were largely attenuated at the measurement surface, the counting efficiency for the deepest source was found to be a factor of 68 times smaller than that of the shallowest source for the "downward-looking" 0–34° collimator. The large deviation from the actual activity of the deepest source for the 475 keV gamma-rays can be attributed to the substantial attenuation at these lower energies. Therefore, the 0–34° measurement of the 475 keV photopeak count rate was not included in the combination reconstruction.

A similar multiple gamma-ray analysis was performed for Setup IV, and the results are displayed in Table 3. For this shallow source setup, there was less attenuating material between

the sources so that the counting efficiencies for the 1365 keV gamma-rays emitted from the deeper sources are no longer insignificant for the larger polar angle collimators. Therefore, contributions from all of the sources were considered for each collimator in the 1365 keV analysis. Due to the reduced attenuation of the 1365 keV gamma-rays, the 60-80° collimator response could no longer solely depend on the shallowest source and was not included in the combination reconstruction.

Most likely, the decreased attenuation of 1365 keV gamma-rays for this shallow setup resulted in the inability of the weakest source to be identified for the separate 1365 keV reconstruction. Recalling for the larger polar angle measurements, the significant attenuation for the deeper sources resulted in small counting efficiencies at the lower gamma-ray energies and lead to simplifications of the response equations, which improved the activity reconstructions. However for the 475 keV, 796 keV, and combination reconstructions, the weakest source was assigned a non-zero activity in between the two stronger sources. In conclusion, the inclusion of multiple gamma-ray emissions into the collimation method improved the activity determinations of the area sources by yielding activities for the deepest sources that were in closer agreement with the actual source activities.

As a general rule, the uncertainties in the reconstructed activities increased with depth, which arises from the fact that the activities and uncertainties of the shallower sources affect the activity determinations of the deeper sources. Although the contributions of the deeper sources could be neglected for some of larger polar angle measurements, the shallowest source still had a significant impact on the smaller polar angle measurements used to characterize the deeper sources. Because the shallower source locations imply greater counting efficiencies than the deeper locations (due to increasing attenuation with depth), the uncertainties in the shallower

sources tended to be magnified in the deeper source activity determinations. The addition of extra measurements has been shown to improve the accuracy of the activity determinations as well as reduce the uncertainty in the activity determinations [20].

Distributed Source Reconstructions

To obtain distributed source reconstructions, the collimation method was applied with an approach that divided the source medium into several depth layers (i.e., discretizing the volume source into layers). Referred to as "distributed source reconstructions," depth distributions were ascertained by determining the source activities within each depth layer. The term "sectioning scheme" refers to how the source medium was divided into depth layers. Different sectioning schemes imply different depth layer thicknesses and/or materials for the same measurement setup and area source arrangement.

The distributed source reconstructions of the collimated measurements, acquired with the ISOCS spectrometry equipment, also used the Monte Carlo calibrations. To verify the capability of the method to assign activity to only those depth layers that include an area source, sectioning schemes were applied to the two-source and three-source setups so that a single depth layer did not contain an area source.

For the purposes of computing the counting efficiencies, the two-source geometry in Fig. 5 was simplified to a concrete slab and divided into three layers with sequential thicknesses of 4, 8, and 12 cm from the surface. Based on a uniform radionuclide distribution within each depth layer, Monte Carlo calibrations of the 796 keV gamma-ray counting efficiencies for each depth layer were computed for the ISOCS spectrometry equipment with the 0–34°, 60–70°, and 70–80° collimators and with a bare detector. The counting efficiency for the deepest layer was over a

factor of 27 times smaller than that for the shallowest depth layer for the bare detector measurement and over a factor of 60 times smaller than that for the shallowest layer for the 60–70°, and 70–80° collimator responses. Therefore, contributions from the deepest layer were only accounted for in the 0–34° collimator response. The counting efficiency for the middle source layer was only a factor of 5, 7, and 12 times smaller than that for the shallowest depth layer for the bare detector, 60–70°, and 70–80° measurements, respectively, and was not neglected. The activities contained within the upper three depth layers were calculated by solving the system of equations for the four measurements, depicted in Eqs. (1)-(3) except that ε represents the counting efficiencies for volume sources (i.e., the depth layers) rather than for area sources. Presented in Table 4(a) and Fig. 8, the activity determinations agreed quite well with the actual activities (within 16%). It is important to note that the reconstruction did not assign activity to the shallowest depth layer, the layer without an area source.

For comparison, another sectioning scheme was applied to the two-source setup where the area sources were located in the center of the two deeper depth layers. The shallowest depth layer did not contain an area source and was unchanged. The middle depth layer was reduced slightly from a concrete thickness of 8 cm to 6.42 cm. The deepest depth layer was also changed from a thickness of 12 cm to 11.36 cm. The results are presented in Table 4(b) and Fig. 8. Sectioning the depth layers so that the area sources were located in middle reduced the 16% underestimation of the middle source to 0% but also decreased the counting efficiency of the deepest depth layer resulting in a 31% overestimation of activity in the deepest depth layer. "Centering" the area sources resulted in an overall improvement in the activities of the upper layers, at the price of a larger percent difference from the actual activity in the deepest layer.

The three-source Setup I in Fig. 6(a) was reduced to a 0.95-cm aluminum plate in front of a 21-cm concrete slab. The shallowest depth layer was defined as the 0.95-cm thick aluminum plate plus 1.05 cm concrete. The next two deeper layers, respectively, were composed entirely of concrete with thicknesses of 6 and 14 cm. Recall, the measurements of Setup I were taken using the ISOCS spectrometry equipment with the bare detector, 0–34°, and 60–80° collimators. Similar to the area source activity reconstructions for Setup I, the 60–80° collimator response was solely used to characterize the activity within the thin shallowest layer, while the deeper two layer's activities were determined from the bare detector and 0–34° collimator measurements. The activity determinations are listed Table 5 and displayed in Fig. 9. For this sectioning scheme, the middle layer did not contain an area source, and correctly, no activity was predicted for that layer.

A distributed source reconstruction was also applied to the three-source Setup III. The source geometry was simplified to consist only of concrete with depth layers of 4, 8, 12-cm thicknesses, respectively for increasing depths (the same sectioning employed with the two-source setup). Displayed in Table 6 and Fig. 10, the activity reconstructions were based on the system of three equations for the bare detector, 0–34°, and 60–80° collimator measurements. While the contributions of the deepest layer were neglected for the bare detector response, the 60–80° collimator response focused on the shallowest depth layer. Even for a simplified geometry consisting only of concrete, the distributed source reconstructions for the Setup III (which actually consisted of concrete, aluminum, and wood) were in agreement with the actual activities. While the shallow and middle layers contained the three area sources, deepest layer was correctly assigned a zero activity. In general, the area sources were not required to be located in the middle of the depth layers to obtain good agreement with the actual activities.

Referring to Fig. 10, the estimated uncertainty in the deepest layer was quite large although a zero activity was correctly assigned. The process used to estimate the uncertainties involved taking the worst case results from all combinations of a 0.95 or 1.05 multiplication factor to each collimator's efficiency. Although the actual worst case resulted in the estimated error bars for the deepest layer to range from 0 – 970 kBq, the case that resulted in an error bar range of 0 –205 kBq seemed more reasonable for the estimated error that the extreme worst case and was, therefore, plotted in Fig. 10. These large error bars at the deepest depths are related to the fact that the measured activities in the deeper layers are very dependent on the activities in the shallower layers. Because the gamma-ray counting efficiencies are smallest for the deepest layers, the uncertainties in the shallower layers tend to be further magnified into the uncertainty of the deepest layer.

Although the area source measurements were still used for the "distributed source reconstruction," activity reconstructions were performed for independent depth layers with a uniform radionuclide distribution (instead of determining the activities of area source at different depths). The relative depth location of the area sources within the depth layers affected the gamma-ray counting efficiencies and could be responsible for significant deviations (because the representation of the source geometry differs so much from the actual setup used in the comparisons). Therefore, the distributed source reconstructions of the area sources should be considered as less than ideal applications of the collimation method. In general, radionuclides tend to be much more widely distributed in most field environments where limited depth distribution information is available. In these more common situations, the distributed source reconstructions become more applicable. It is important to note that the area sources were not required to be located in the middle of the depth layers to obtain good agreement with the actual

activities. Overall, the collimation method preserved the qualitative shapes of the actual depth distributions for each of experimental setups (even for non-monotonic depth distributions).

Conclusions

Area sources of ^{134}Cs were placed at various depths in attenuating materials to test the ability of the presented collimation method to determine depth information. Using the HPGe detector with the Monte Carlo calibration, the collimation method determined the activities of the shallowest area sources to within 10% of their actual activities. The method had trouble identifying the presence of the weakest source located in between and in close proximity to the more active sources. Except for those instances where the weakest source was not identified in between the stronger sources, the area source activities were determined to within 26% for the middle source and within 82% for the deepest source. In general, greater deviations from the actual source activities were realized for the deepest source depths. The advantages of the collimation method over other *in situ* methods has been discussed [14, 20].

The activity reconstructions from Monte Carlo calibrations of the HPGe detector were compared to those from the experimental calibration of a NaI(Tl) detector [14]. The two combinations of calibration approach and spectrometer equipment exhibited similar accuracies. Although neither calibration/equipment combination was determined to be superior, it was concluded that the presented collimation method could be implemented using either the experimental or Monte Carlo calibrations. Of the two detectors, however, the HPGe detector is far more practical for conducting actual field measurements due to its superior energy resolution. In the common situation of complex gamma-ray backgrounds due the presence of multiple radionuclides, fine energy resolution is crucial for distinguishing the individual gamma-ray

emissions and radionuclides. For the same reason, the HPGe detector is also more appropriate for the analyses of multiple gamma-ray emissions, which were shown to improve the activity reconstructions when compared the analysis using a single gamma-ray emission. Having demonstrated its flexibility with different collimators and measurement geometries, the Monte Carlo calibration also offers the significant advantage of not requiring custom-made area sources for experimental calibrations.

Paired with the ISOCS system, the collimation method represents a fast and effective approach for determining radionuclide depth distributions in realistic environments. The ability to obtain depth distribution from *in situ* measurements alleviates the need to acquire, prepare, and analyze core samples. With basic knowledge of the gamma-ray attenuation properties (i.e., materials and densities) from the area of interest, the combination of the collimation method with the ISOCS system represents an independent tool for quantifying gamma-ray emitting radionuclides in materials.

Acknowledgements

The authors are grateful to Frazier Bronson of Canberra Industries, Inc., who loaned the high-purity germanium spectroscopy system for this work. Charlie Weger, Joe Miklos, and Christopher Becker deserve recognition for their assistance with fabricating of the lead collimators, creating the area sources, and providing a liquid nitrogen source, respectively. Dr. James Holloway, Dr. Zhong He, Dr. Avery Demond, and Dr. Ronald Fleming are thanked for their suggestions. A portion of this research was performed under appointment to the Civilian Radioactive Waste Management Fellowship program administered by the Oak Ridge Institute for Science and Education under contract number DE-AC05-76OR00033 between the U.S. Department of Energy and the Oak Ridge Associated Universities.

Footnotes

[1] *In Situ* Object Counting System (ISOCS) is a trademark of Canberra Industries, Inc., 800 Research Parkway, Meriden, CT 06450.

[2] Briemeister, J. F. (ed.), MCNP – A general Monte Carlo N-Particle transport code, Version 4a. Report LA-12625-M, Los Alamos National Laboratory, November 1993.

[3] *In Situ* Object Counting System (ISOCS):
Canberra Industries, Inc., 800 Research Parkway, Meriden, CT 06450.
Spectroscopy Equipment:
High-Purity Germanium (HPGe) p-type coaxial detector, 40% relative efficiency
Big Multi-Attitude Cryostat (MAC), features a larger dewar with a 5-day liquid nitrogen holding time
Inspector Multichannel Analyzer, 8192 channels
Software:
ISOCS Calibration Software, installed on an IBM ThinkPad 365XD laptop computer
Genie-2000 Counting Software, installed on an IBM ThinkPad 365XD laptop computer

[4] Validation and Internal Consistency Testing of ISOCS Efficiency Calibration. Manual 9231205C; 9/99. Canberra Industries, Inc., 800 Research Parkway, Meriden, CT 06450.

[5] Canberra Industries, Inc., 800 Research Parkway, Meriden, CT 06450.

[6] Model S573 ISOCS Calibration Software. User's Manual 9231013B; 8/99. Canberra Industries, Inc., 800 Research Parkway, Meriden, CT 06450.

References

[1] L. R. Anspaugh, IEEE Trans. Nucl. Sci. NS-23, 3 (1976) 1190-1196.

[2] W. Sowa, E. Martini, K. Gehrcke, P. Marschner, M. J. Naziry, Radiat. Prot. Dosim. 27, 2 (1989) 93-101.

[3] S. H. Fong, J. L. Alvarez, Health Phys. 72, 2 (1997) 286-295.

[4] M. Korun, R. Martinčič, B. Pucelj, Nucl. Instrum. Methods Phys. Res. A 300 (1991) 611-615.

[5] K. Rybacek, P. Jacob, R. Meckbach, Health Phys. 62, 2 (1992) 519-528.

[6] K. M. Miller, P. Shebell, G. A. Klemic, Health Phys. 67 (1994) 140-150.

[7] E. P. Naessens, X. G. Xu, Health Phys. 77, 1 (1999) 76-88.

[8] P. Zombori, A. Andrási, I. Németh, A new method for the determination of radionuclide distribution in the soil by in situ gamma-ray spectrometry. Budapest, Hungary: Central Research Institute for Physics, Institute for Atomic Energy Research. KFKI-1992-20/K, 1992.

[9] A. N. Tyler, D. C. W. Sanderson, E. M. Scott, J. Environ. Radioactivity 33, 3 (1996) 195-212.

[10] A. N. Tyler, J. Environ. Radioactivity 45 (1999) 235-252.

[11] A. V. Chesnokov, V. I. Fedin, A. P. Govorun, O. P. Ivanov, V. I. Liksonov, V. N. Potapov, S. V. Smirnov, S. B. Shcherbak, L. I. Urutskoev, Appl. Radiat. Isot. 48, 9 (1997) 1265-1272.

[12] V. N. Golosov, D. E. Walling, E. V. Kvasnikova, E. D. Stukin, A. N. Nikolaev, A. V. Panin, J. Environ. Radioactivity 48 (2000) 79-94.

[13] M. Korun, A. Likar, M. Lipoglavšek, R. Martinčič, B. Pucelj, Nucl. Instrum. Methods Phys. Res. B 93 (1994) 485-491.

[14] R. R. Benke, K. J. Kearfott, Nucl. Instrum. Methods Phys. Res. A (accepted January 8, 2001)

[15] M. Fülöp, P. Ragan, Health Phys. 72 (1997) 923-930.

[16] A. Likar, T. Vidmar, B. Pucelj, Health Phys. 75 (1998) 165-169.

[17] K. Saito, P. Jacob, Radiat. Prot. Dosim. 58 (1995) 29-45.

[18] A. Clouvas, S. Xanthos, M. Antonopoulos-Domis, J. Silva, Health Phys. 74 (1998) 216-230.

[19] A. Clouvas, S. Xanthos, M. Antonopoulos-Domis, J. Silva, Health Phys. 78 (2000) 295-302, Coorespondence in Health Phys. 79 (2000) 614-616.

[20] R. R. Benke, An improved method for determining radionuclide depth distributions using *in situ* gamma-ray spectrometry. Ph.D. Dissertation, The University of Michigan: Ann Arbor, MI, 2000.

Table 1(a). Actual and measured activities of three area sources at different depths for Setup I. Shown in Fig. 6(a), the area sources C, B, and A, respectively, were positioned at increasing depths from the surface. The measured activities were determined from three measurements using the ISOCS spectrometry equipment with the 0–34° and 60–80° collimators and a bare detector measurement. The presented uncertainties in the actual activities of the area sources are estimated 2σ values. The presented uncertainties in the measured activities are estimated values for the worst case results due to a 5% uncertainty applied to each collimator's efficiency. The measured activities in parentheses represent the range in the measured activities due to the estimated uncertainties. The percent differences were computed as 100%*(Measured activity – Actual activity)/(Actual activity).

Source	Actual Activity (kBq)	Measured Activity (kBq)	Percent Difference
C	28 ± 3	29 (27 – 30)	+3.6%
B	130 ± 14	150 (110 – 190)	+15%
A	520 ± 33	810 (480 – 1100)	+56%

Table 1(b). Activity determinations for the three sources at different depths in Setup II. Shown in Fig. 6(b), the area sources A, C, and B, respectively, were positioned at increasing depths from the surface. Listed in the "excluding bare measurement" column, the measured activities were determined from three measurements using the ISOCS spectrometry equipment using the 0–34°, 42–60°, 60–80° collimators. To assess the impact of taking an additional measurement (four measurements for three sources), a bare detector measurement was combined with the three collimated measurements for a new activity reconstruction, listed in the "including bare measurement" column. The presented uncertainties in the actual activities of the area sources are estimated 2σ values. The presented uncertainties in the measured activities are estimated values for the worst case results due to a 5% uncertainty applied to each collimator's efficiency. The measured activities in parentheses represent the range in the measured activities due to the estimated uncertainties. The percent differences were computed as 100%*(Measured activity – Actual activity)/(Actual activity).

	Activities (kBq)				
Source	Actual	Excluding Bare Measurement	Percent Difference	Including Bare Measurement	Percent Difference
A	510 ± 32	500 (480 – 530)	-2.0%	500 (480 – 530)	-2.0%
C	27 ± 3	0 (0 – 0)	-100%	0 (0 – 290)	-100%
B	130 ± 14	0 (0 – 170)	-100%	24 (0 – 380)	-82%

Table 1(c). Actual and measured activities of the three area sources at different depths for Setup III. Shown in Fig. 6(c), the area sources A, C, and B, respectively, were positioned at increasing depths from the surface. The measured activities were determined from three measurements using the ISOCS spectrometry equipment with the 0–34°, 42–60°, 60–80° collimators. The presented uncertainties in the actual activities of the area sources are estimated 2σ values. The presented uncertainties in the measured activities are estimated values for the worst case results due to a 5% uncertainty applied to each collimator's efficiency. The measured activities in parentheses represent the range in the measured activities due to the estimated uncertainties. The percent differences were computed as 100%*(Measured activity – Actual activity)/(Actual activity).

Source	Actual Activity (kBq)	Measured Activity (kBq)	Percent Difference
A	520 ± 33	470 (450 – 500)	-9.6%
C	28 ± 3	0 (0 – 0)	-100%
B	130 ± 14	130 (0 – 385)	0%

Table 1(d). Actual and measured activities of three area sources at different depths for the Setup IV. Shown in Fig. 6(d), the area sources B, C, and A, respectively, were positioned at increasing depths from the surface. Listed in the "excluding 42–60° measurement column, the measured activities were determined from three measurements using the ISOCS spectrometry equipment with the 0–34° and 60–80° collimators and a bare detector measurement. To assess the impact of taking an additional measurement (four measurements for three sources), a 42–60° collimator measurement was added for a new activity reconstruction, shown in the "including 42–60° measurement" column. The presented uncertainties in the actual activities of the area sources are estimated 2σ values. The presented uncertainties in the measured activities are estimated values for the worst case results due to a 5% uncertainty applied to each collimator's efficiency. The measured activities in parentheses represent the range in the measured activities due to the estimated uncertainties. The percent differences were computed as 100%*(Measured activity – Actual activity)/(Actual activity).

	Activities (kBq)				
Source	Actual	Excluding 42-60° Measurement	Percent Difference	Including 42-60° Measurement	Percent Difference
B	126 ± 14	125 (119 – 132)	-0.79%	125 (119 – 132)	-0.79%
C	27 ± 3	120 (83 – 160)	+340%	34 (0 – 71)	+26%
A	510 ± 32	360 (190 – 540)	-29%	660 (500 – 810)	+29%

Table 2. Activity determinations from multiple gamma-ray energies for Setup I, shown in Fig. 6(a). The activities were determined from three measurements using the ISOCS spectrometry equipment with the 0–34° and 60–80° collimators and a bare detector measurement. The data from all three gamma-ray energies were incorporated into a single activity determination, dictated by Eqs. (2) and (3) and referred to as the "combination activities." The presented uncertainties in the actual activities of the area sources are estimated 2σ values. The percentages in parentheses represent the percent deviation from the actual activity.

Actual Source Activities (kBq)	475 keV Activities (kBq)	796 keV Activities (kBq)	1365 keV Activities (kBq)	Combination Activities (kBq)
28 ± 3	25 (-11%)	29 (+3.6%)	37 (+32%)	29 (+3.6%)
130 ± 14	140 (+7.7%)	150 (+15%)	140 (+7.7%)	150 (+15%)
520 ± 33	1400 (+170%)	810 (+56%)	530 (+1.9%)	780 (+50%)

Table 3. Activity determinations from multiple gamma-ray energies for Setup IV, shown in Fig. 6(d). The activities were determined from four measurements using the ISOCS spectrometry equipment with the 0–34°, 42–60°, and 60–80° collimators and a bare detector measurement. The data from all three gamma-ray energies were incorporated into a single activity determination, dictated by Eqs. (2) and (3) and referred to as the "combination activities." The presented uncertainties in the actual activities of the area sources are estimated 2σ values. The percentages in parentheses represent the percent deviation from the actual activity.

Actual Source Activities (kBq)	475 keV Activities (kBq)	796 keV Activities (kBq)	1365 keV Activities (kBq)	Combination Activities (kBq)
126 ± 14	102 (-19%)	125 (-0.79%)	140 (+11%)	125 (-0.79%)
27 ± 3	56 (+110%)	34 (+26%)	0 (-100%)	34 (+26%)
510 ± 32	840 (+65%)	660 (+29%)	540 (+5.9%)	650 (+27%)

Table 4. Actual and measured activities for a distributed source reconstruction of the two-source setup, shown in Fig. 5. In addition to a bare detector measurement, the ISOCS spectrometry equipment was used with the 0–34°, 60–70°, and 70–80° collimator. The counting efficiencies were calculated using the ISOCS calibration software for a uniform radionuclide distribution in the concrete layers. Two sectioning schemes were employed: (a) for layer thicknesses of 4, 8, and 12 cm, respectively at increasing depths, and (b) for area sources located in the middle of the depth layers with thicknesses of 4, 10.42, and 11.36 cm, respectively at increasing depths. For both sectioning schemes the shallowest layer did not contain an area source. However, the middle layer contained Source B, and the deepest layer contained Source A. The presented uncertainties in the actual activities are estimated 2σ values for the area source(s) contained with the depth layer. The presented uncertainties in the measured activities are estimated values for the worst case results due to a 5% uncertainty applied to each collimator's efficiency. The measured activities in parentheses represent the range in the measured activities due to the estimated uncertainties. The percent differences were computed as 100%*(Measured activity – Actual activity)/(Actual activity).

(a)

Layer Depths (cm)	Actual Activity (kBq)	Measured Activity (kBq)	Percent Difference
0 – 4	0	0 (0 – 0)	0%
4 – 12	128 ± 14	107 (102 – 113)	-16%
12 – 24	520 ± 33	470 (400 – 560)	-9.6%

(b)

Layer Depths (cm)	Actual Activity (kBq)	Measured Activity (kBq)	Percent Difference
0 – 4	0	0 (0 – 0)	0%
4 – 14.42	128 ± 14	128 (122 – 135)	0%
14.42 – 25.78	520 ± 33	680 (560 – 800)	+31%

Table 5. Actual and measured activities for a distributed source reconstruction of three-source Setup I, shown in Fig. 6(a). Counting efficiencies were calculated using the ISOCS calibration software for uniform distributions of radionuclides within layers of 0.95-cm aluminum plus 1.05-cm of concrete, 6-cm concrete, and 14-cm concrete, respectively at increasing depths. The shallowest layer contained Source C. The middle layer did not contain an area source, and the deepest layer contained Sources B and A. The presented uncertainties in the actual activities are estimated 2σ values for the area source(s) contained with the depth layer. The presented uncertainties in the measured activities are estimated values for the worst case results due to a 5% uncertainty applied to each collimator's efficiency. The measured activities in parentheses represent the range in the measured activities due to the estimated uncertainties. The percent differences were computed as 100%*(Measured activity – Actual activity)/(Actual activity).

Layer Depths (cm)	Actual Activity (kBq)	Measured Activity (kBq)	Percent Difference
0 – 2	28 ± 3	16 (14 – 18)	-43%
2 – 8	0	0 (0 – 0)	0%
8 – 22	650 ± 36	520 (480 – 550)	-20%

Table 6. Actual and measured activities for a distributed source reconstruction of the three-source Setup III, shown in Fig. 6(c). A simplified model of the source geometry, consisting only of concrete, was employed. Counting efficiencies were calculated for uniform distributions of radionuclides within concrete layers at increasing depths with thicknesses of 4, 8, and 12 cm, respectively. The 0 – 4 cm layer contained Source A. When the increased attenuation of the aluminum and reduced attenuation of the wood layers are converted to equivalent thicknesses of concrete, the 4 – 12 cm layer contains Sources C and B, while the 12 – 24 cm layer does not contain an area source. The presented uncertainties in the actual activities are estimated 2σ values for the area source(s) contained with the depth layer. The presented uncertainties in the measured activities are estimated values for the worst case results due to a 5% uncertainty applied to each collimator's efficiency. The measured activities in parentheses represent the range in the measured activities due to the estimated uncertainties. The percent differences were computed as 100%*(Measured activity – Actual activity)/(Actual activity).

Layer Depths (cm)	Actual Activity (kBq)	Measured Activity (kBq)	Percent Difference
0 – 4	520 ± 33	480 (460 – 520)	-7.7%
4 – 12	160 ± 14	150 (0 – 277)	-6.3%
12 – 24	0	0 (0 – 205)	0%

Figure Captions

Fig. 1(a). Cross-sectional diagram of the dimensions for the 0-34° collimator. All dimensions are in centimeters.

Fig. 1(b). Cross-sectional diagram of the dimensions for the 42-60° collimator. All dimensions are in centimeters.

Fig. 1(c). Cross-sectional diagram of the dimensions for the 60-70° collimator. All dimensions are in centimeters.

Fig. 1(d). Cross-sectional diagram of the dimensions for the 70-80° collimator. All dimensions are in centimeters.

Fig. 2. Cross-sectional diagram of the 42-60° collimator indicating the regions where the edges were extended for input into the ISOCS calibration software. Refer to Fig. 1(b) for the other dimensions of the collimator.

Fig. 3. Experimental setup for the full geometry: (a) top view and (b) side view including a cross-sectional view of the collimator. The full geometry was used for the 0-34° collimator measurements.

Fig. 4. Experimental setup for the ¼ geometry: (a) top view and (b) side view including a cross-sectional view of the collimator. Note that when the count rate data obtained from measurements of the ¼ geometry are multiplied by four, it is equivalent to a measuring a source four times greater in area. The ¼ geometry allowed for more manageable sizes of the area sources (1.02 m by 1.02 m), reduced the amount of repetitive attenuating material, and consumed less laboratory space. The ¼ geometry was used for all collimator measurements except the 0-34° measurements.

Fig. 5. Attenuating materials and source locations for a two-source geometry. The presented dimensions represent the material thickness. The wood thickness of each source layer is 0.5 cm.

Fig. 6(a). Attenuating materials and source locations for the three-source Setup I. The presented dimensions represent the material thickness. For proper alignment and improved stability, Sources B and C were attached to larger plywood boards with a thickness of 1.2 cm. The wood thickness of each source layer is 0.5 cm.

Fig. 6(b). Attenuating materials and source locations for the three-source Setup II. The presented dimensions represent the material thickness. Note the small amount of attenuating material between Sources C and B (equivalent to only 2.0 cm of soil or 1.6 cm of concrete for 796 keV gamma-rays). The wood thickness of each source layer is 0.5 cm.

Fig. 6(c). Attenuating materials and source locations for the three-source Setup III. The presented dimensions represent the material thickness. Note the small amount of attenuating material between Sources C and B. The wood thickness of each source layer is 0.5 cm.

Fig. 6(d). Attenuating materials and source locations for the three-source Setup IV. The presented dimensions represent the material thickness. Note the small amount of attenuating material between Sources B and C (equivalent to only 2.8 cm of soil or 2.2 cm of concrete for 796 keV gamma-rays). The wood thickness of each source layer is 0.5 cm.

Fig. 7(a). Actual and measured activities of three area sources at different depths for Setup I corresponding to Table 1(a). Shown in Fig. 6(a), the area sources C, B, and A, respectively, were positioned at increasing depths from the surface. The measured activities were determined from three measurements using the ISOCS spectrometry equipment with the 0–34° and 60–80° collimators as well as from a bare detector measurement. The presented uncertainties in the measured activities are estimated values for the worst case results due to a 5% uncertainty applied to each collimator's efficiency. The presented uncertainties in the actual activities of the area sources are estimated 2σ values.

Fig. 7(b). Activity determinations for the three sources at different depths in Setup II corresponding to Table 1(b). Shown in Fig. 6(b), the area sources A, C, and B, respectively, were positioned at increasing depths from the surface. The "3 Measurements" case used the ISOCS spectrometry equipment with the 0–34°, 42–60°, and 60–80° collimators. The "4 Measurements" case added a bare detector measurement. The presented uncertainties in the measured activities are estimated values for the worst case results due to a 5% uncertainty applied to each collimator's efficiency. The presented uncertainties in the actual activities of the area sources are estimated 2σ values.

Fig. 7(c). Actual and measured activities of three area sources at different depths for Setup III corresponding to Table 1(c). Compared to Setup II, the locations of the 0.95-cm and 1.27-cm aluminum layers were switched and the 1.9-cm wood layer was moved from above Source C to directly above Source B. For Setup III shown in Fig. 6(c), the area sources A, C, and B, respectively, were positioned at increasing depths from the surface. The measured activities were determined from three measurements using the ISOCS spectrometry equipment with the 0–34°, 42–60°, and 60–80° collimators. The presented uncertainties in the measured activities are estimated values for the worst case results due to a 5% uncertainty applied to each collimator's efficiency. The presented uncertainties in the actual activities of the area sources are estimated 2σ values.

Fig. 7(d). Actual and measured activities of three area sources at different depths for the Setup IV corresponding to Table 1(d). Shown in Fig. 6(d), the area sources B, C, and A, respectively, were positioned at increasing depths from the surface. The "3 Measurements" case used the ISOCS spectrometry equipment with the 0–34° and 60–80° collimators and a bare detector measurement. The "4 Measurements" case added a 42–60° collimator measurement. The presented uncertainties in the measured activities are estimated values for the worst case results

due to a 5% uncertainty applied to each collimator's efficiency. The presented uncertainties in the actual activities of the area sources are estimated 2σ values.

Fig. 8. Actual and measured activities, corresponding to Table 4, for a distributed source reconstruction of the two-source setup, shown in Fig. 5. In addition to a bare detector measurement, the ISOCS spectrometry equipment was used with the 0–34°, 60–70°, and 70–80° collimator. The counting efficiencies were calculated using the ISOCS calibration software for a uniform radionuclide distribution in the concrete layers. Two sectioning schemes were employed: (a) for layer thicknesses of 4, 8, and 12 cm, respectively at increasing depths, and (b) for area sources "centered" within the depth layers with thicknesses of 4, 10.42, and 11.36 cm, respectively at increasing depths. The presented uncertainties in the measured activities are estimated values for the worst case results due to a 5% uncertainty applied to each collimator's efficiency. The presented uncertainties in the actual activities of the area sources are estimated 2σ values.

Fig. 9. Actual and measured activities a distributed source reconstruction of Setup I, corresponding to Table 5. Measurements were acquired using the ISOCS spectrometry equipment with the bare detector, 0–34°, and 60–80° collimators. The counting efficiencies were calculated using the ISOCS calibration software for uniform distributions of radionuclides within layers of 0.95-cm aluminum plus 1.05 cm of concrete, 6-cm concrete, and 14-cm concrete, respectively at increasing depths. The shallowest layer contained Source C. The middle layer did not contain an area source, and the deepest layer contained Sources B and A. The presented uncertainties in the measured activities are estimated values for the worst case results due to a 5% uncertainty applied to each collimator's efficiency. The presented uncertainties in the actual activities of the area sources are estimated 2σ values.

Fig. 10. Actual and measured activities for a distributed source reconstruction of the three-source Setup III, corresponding to Table 6. Measurements were acquired using the ISOCS spectrometry system. A simplified model of the source geometry, consisting only of concrete, was employed. Counting efficiencies were calculated for uniform distributions of radionuclides within concrete layers at increasing depths with thicknesses of 4, 8, and 12 cm, respectively. The 0 – 4 cm layer contained Source A. When the increased attenuation of the aluminum and reduced attenuation of the wood layers are converted to equivalent thicknesses of concrete, the 4 – 12 cm layer contains Sources C and B, while the 12 – 24 cm layer does not contain an area source. The presented uncertainties in the measured activities are estimated values for the worst case results due to a 5% uncertainty applied to each collimator's efficiency. The presented uncertainties in the actual activities of the area sources are estimated 2σ values.

Fig. 1(a).

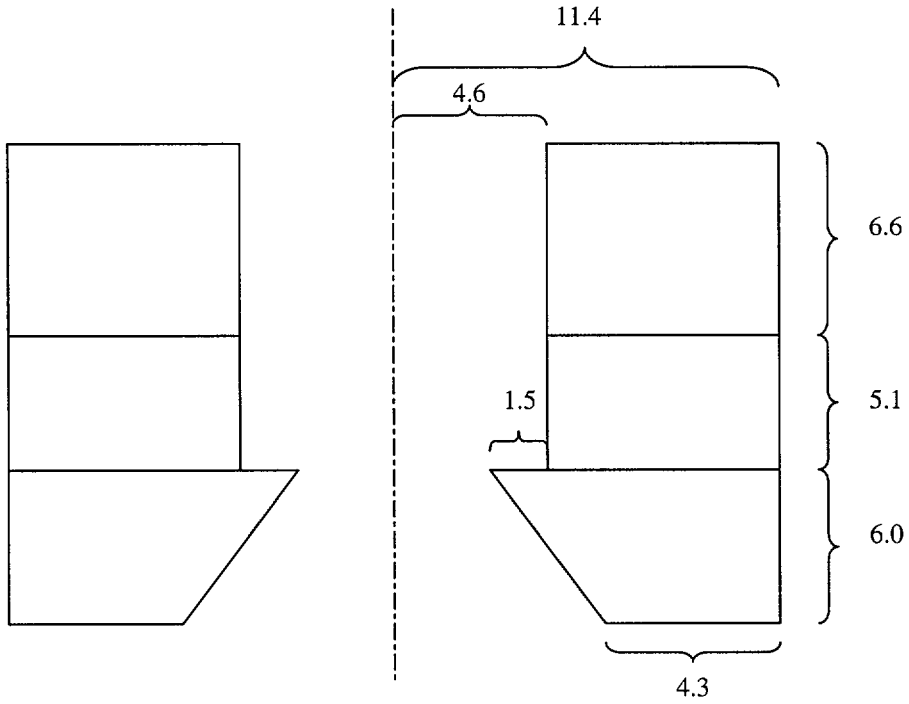

Fig. 1(b).

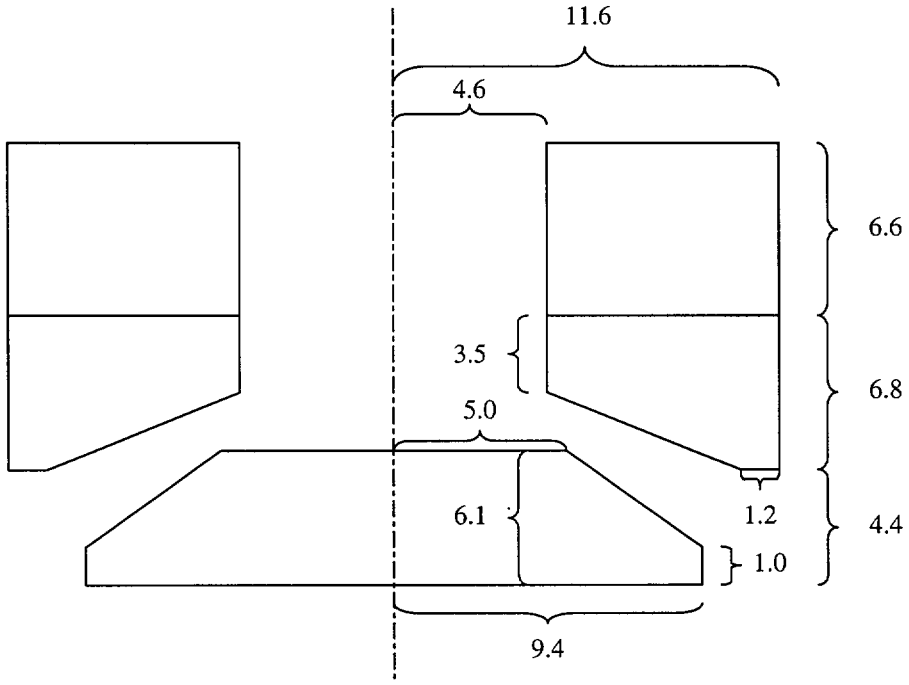

Fig. 1(c).

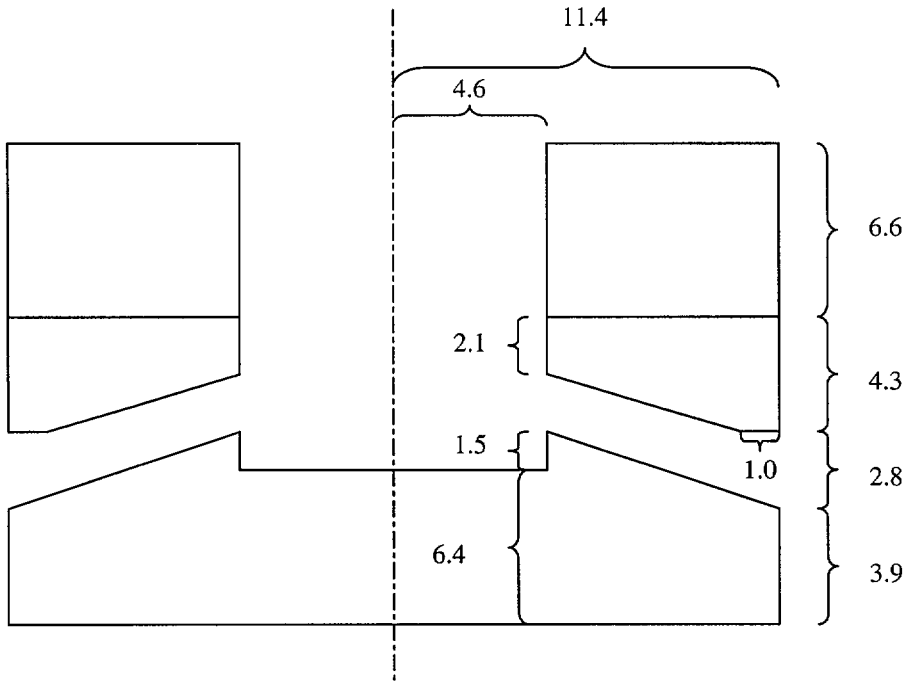

Fig. 1(d).

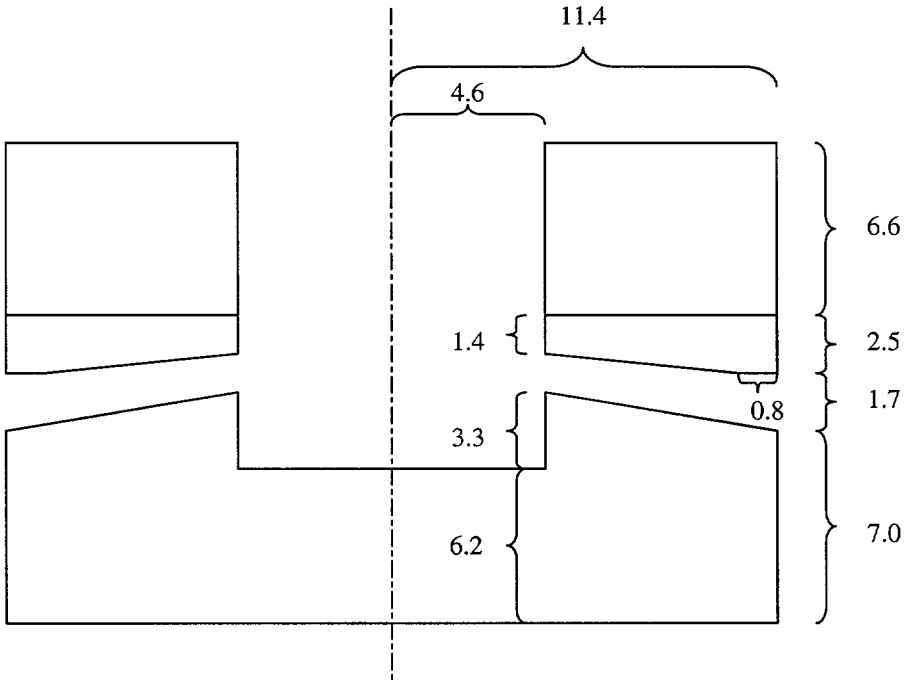

Fig. 2.

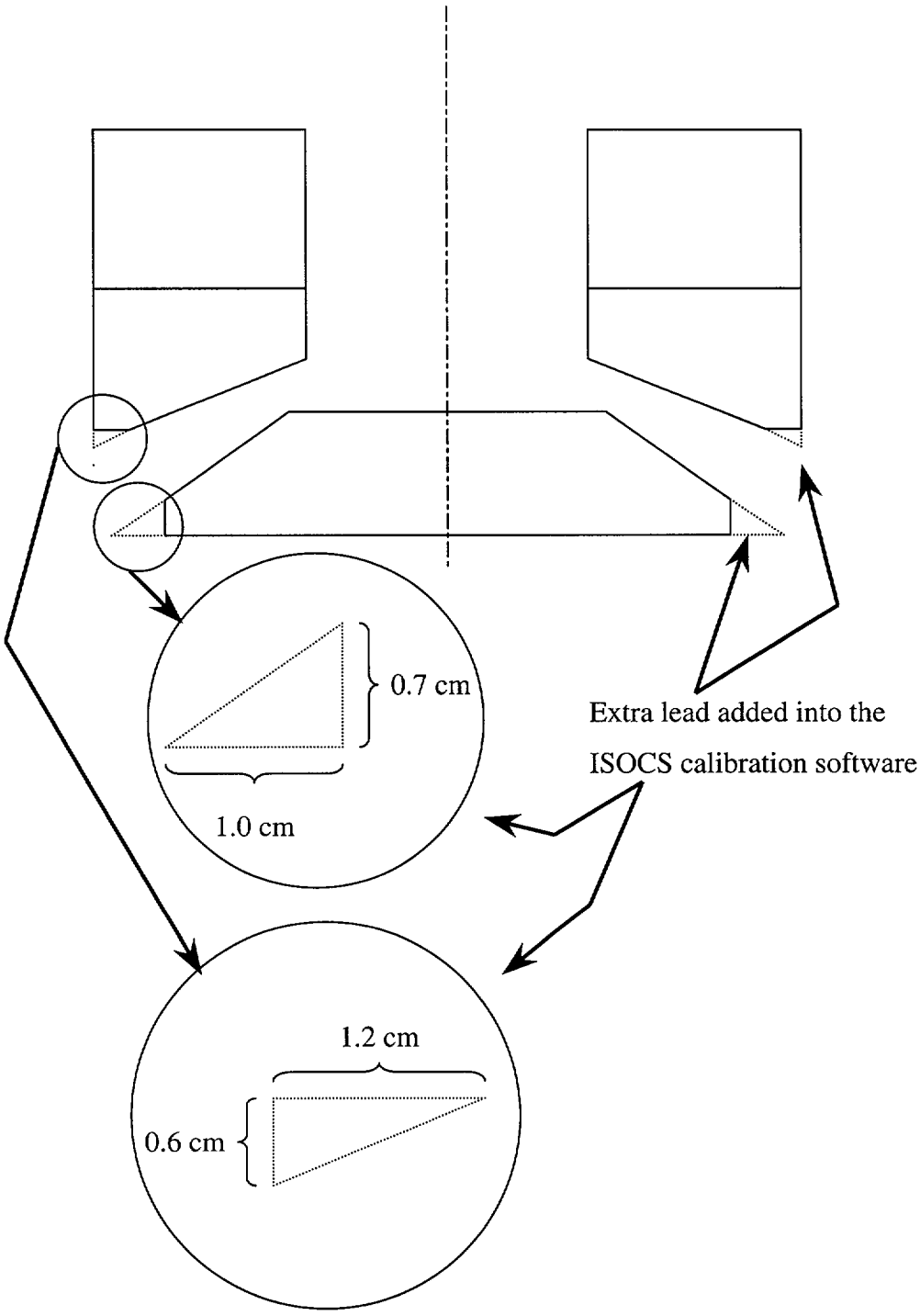
0.7 cm
1.0 cm
Extra lead added into the
ISOCS calibration software
1.2 cm
0.6 cm

Fig. 3.

(a)

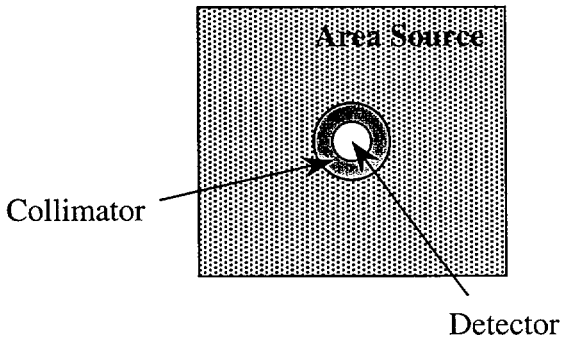
Area Source
Collimator
Detector

(b)

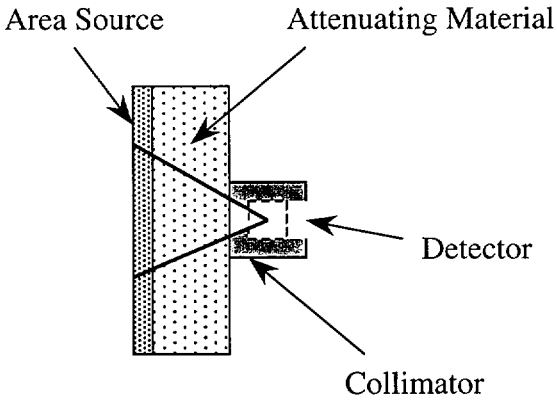
Area Source
Attenuating Material
Detector
Collimator

Fig. 4.

(a)

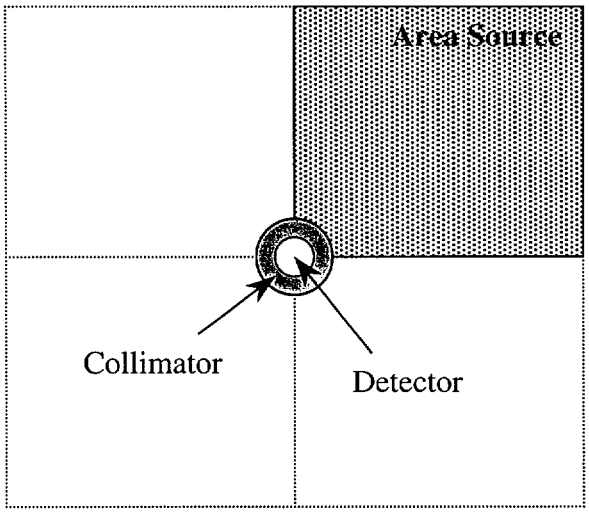
Area Source
Collimator
Detector

(b)

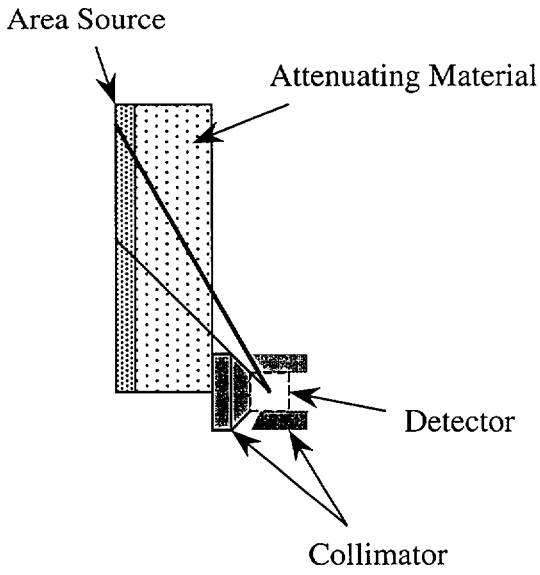
Area Source
Attenuating Material
Detector
Collimator

Fig. 5.

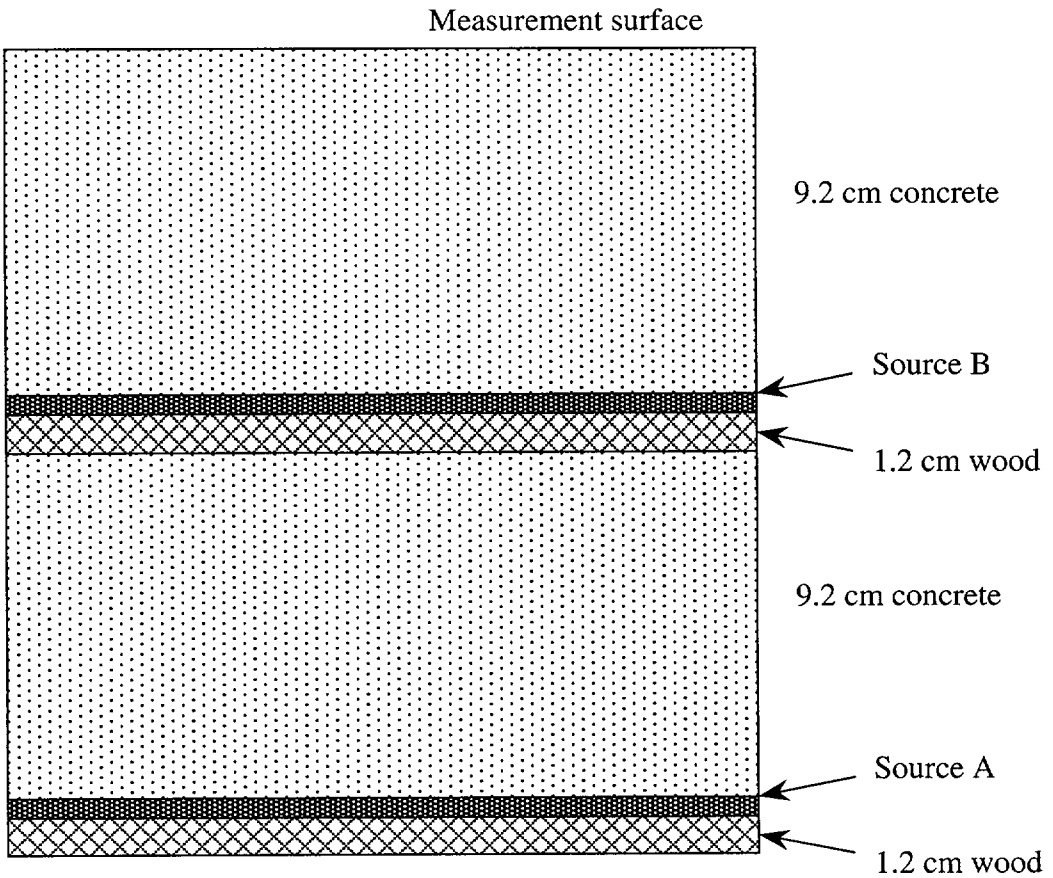
Measurement surface
9.2 cm concrete
Source B
1.2 cm wood
9.2 cm concrete
Source A
1.2 cm wood

Fig. 6(a).

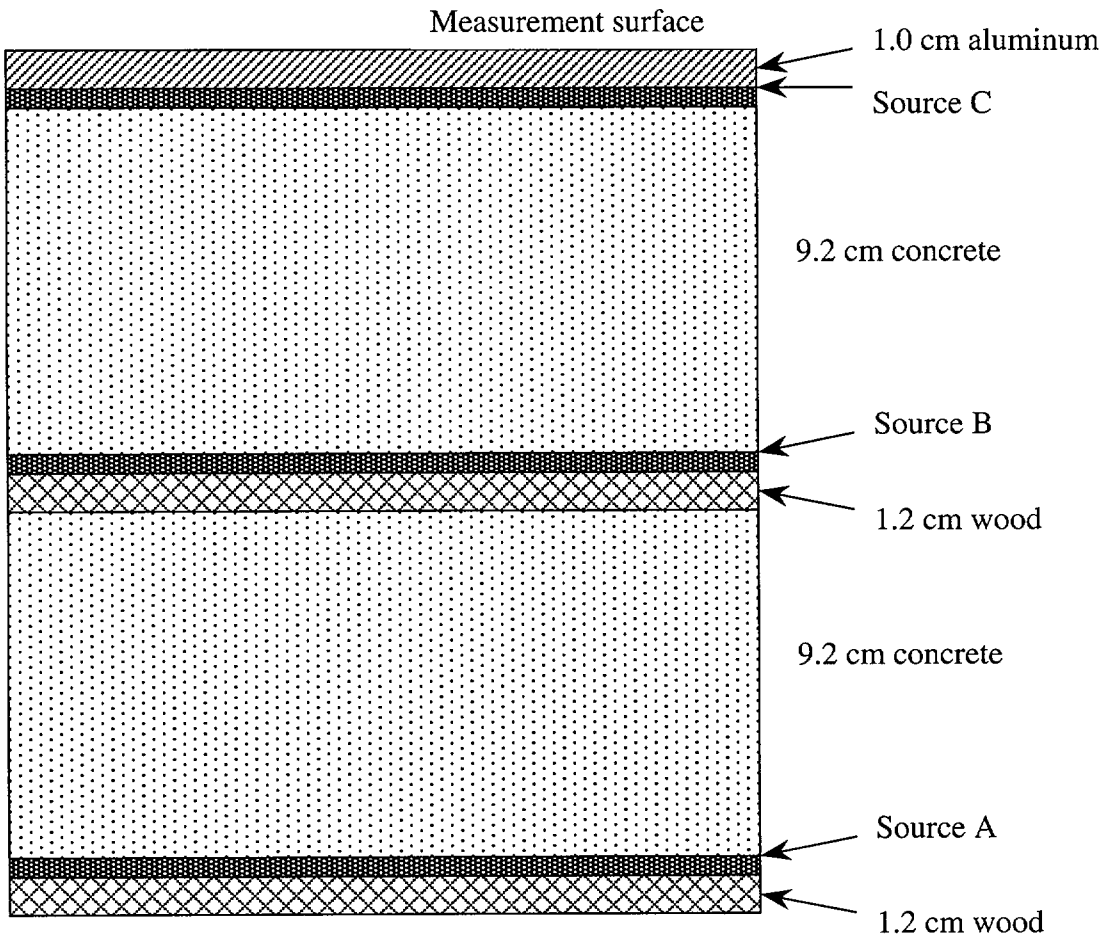
Measurement surface
1.0 cm aluminum
Source C
9.2 cm concrete
Source B
1.2 cm wood
9.2 cm concrete
Source A
1.2 cm wood

Fig. 6(b).

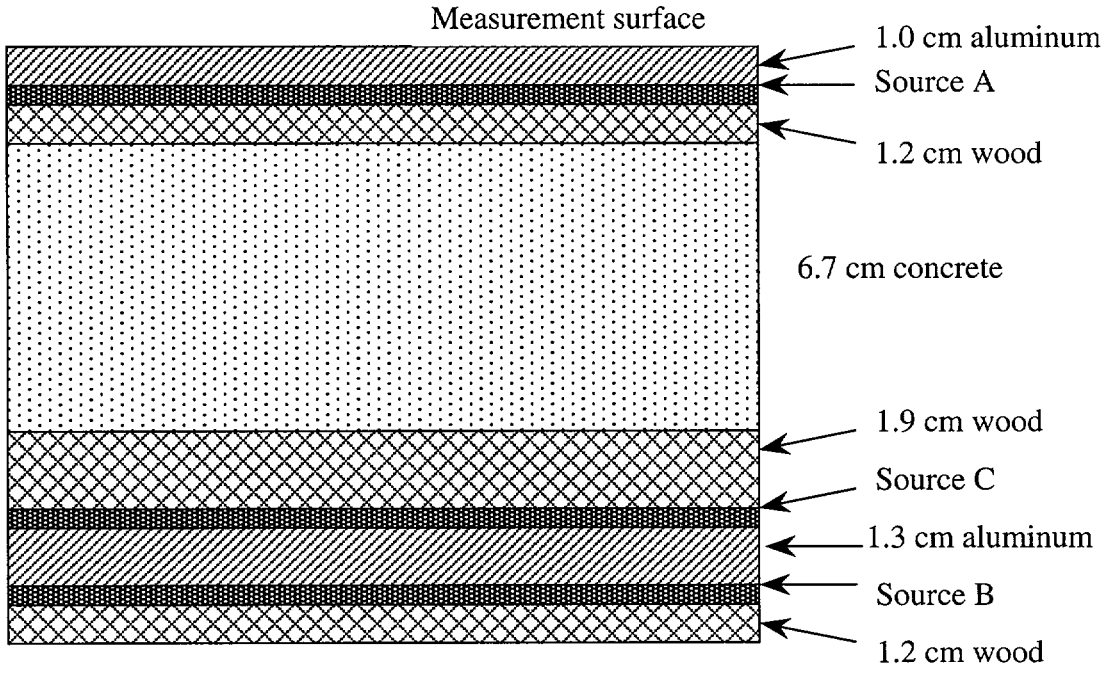
Measurement surface
1.0 cm aluminum
Source A
1.2 cm wood
6.7 cm concrete
1.9 cm wood
Source C
1.3 cm aluminum
Source B
1.2 cm wood

Fig. 6(c).

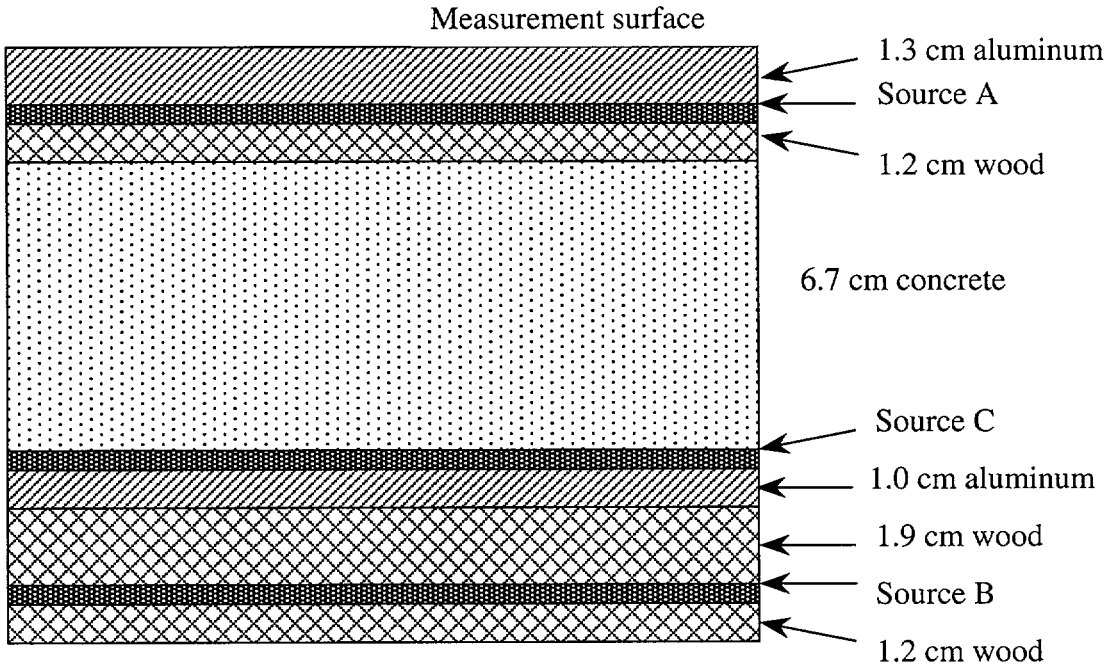
Measurement surface
1.3 cm aluminum
Source A
1.2 cm wood
6.7 cm concrete
Source C
1.0 cm aluminum
1.9 cm wood
Source B
1.2 cm wood

Fig. 6(d).

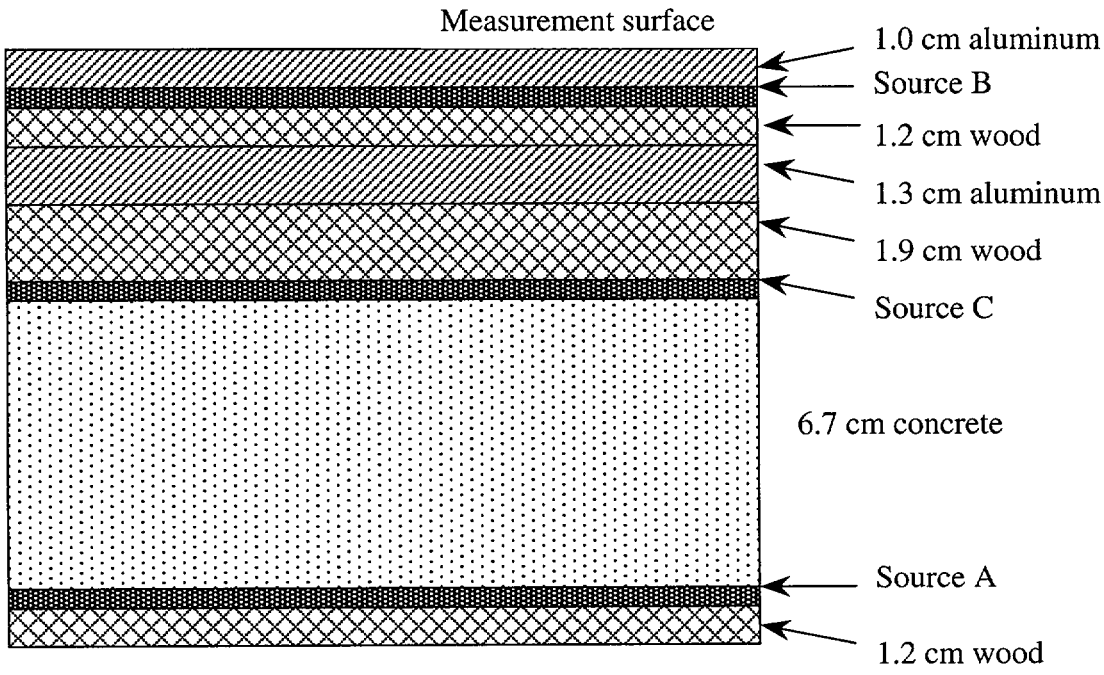
Measurement surface
1.0 cm aluminum
Source B
1.2 cm wood
1.3 cm aluminum
1.9 cm wood
Source C
6.7 cm concrete
Source A
1.2 cm wood

Fig. 7(a).

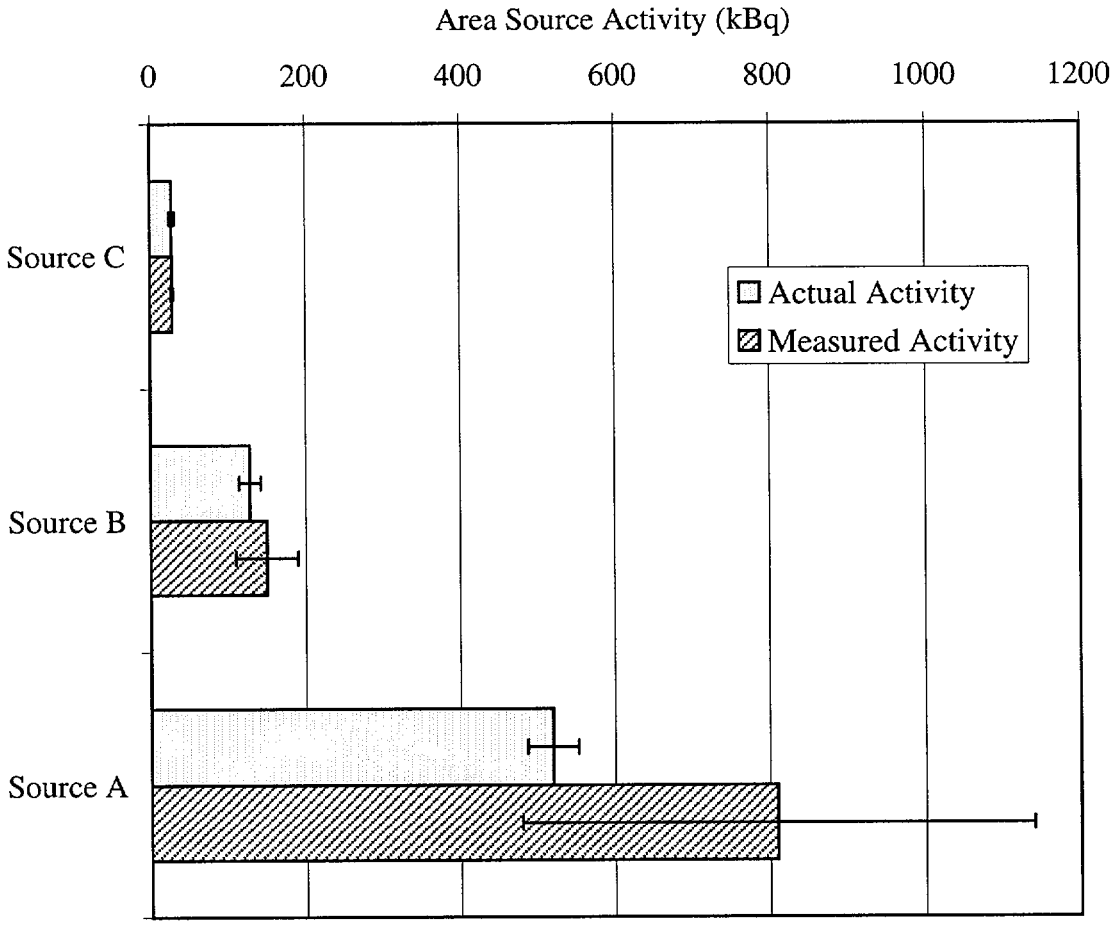
Area Source Activity (kBq)
0
200
400
600
800
1000
1200
Source C
Source B
Source A
Actual Activity
Measured Activity

Fig. 7(b).

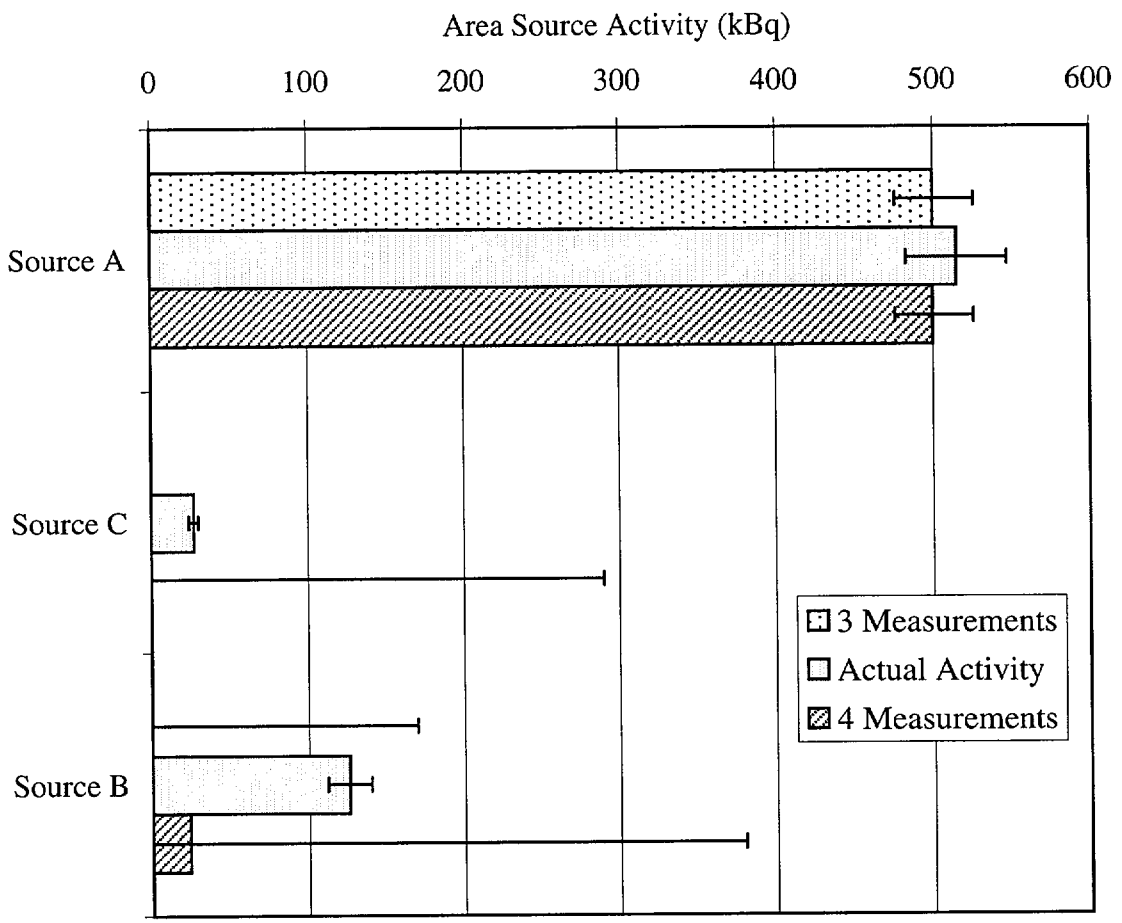
Area Source Activity (kBq)
0
100
200
300
400
500
600
Source A
Source C
Source B
3 Measurements
Actual Activity
4 Measurements

Fig. 7(c).

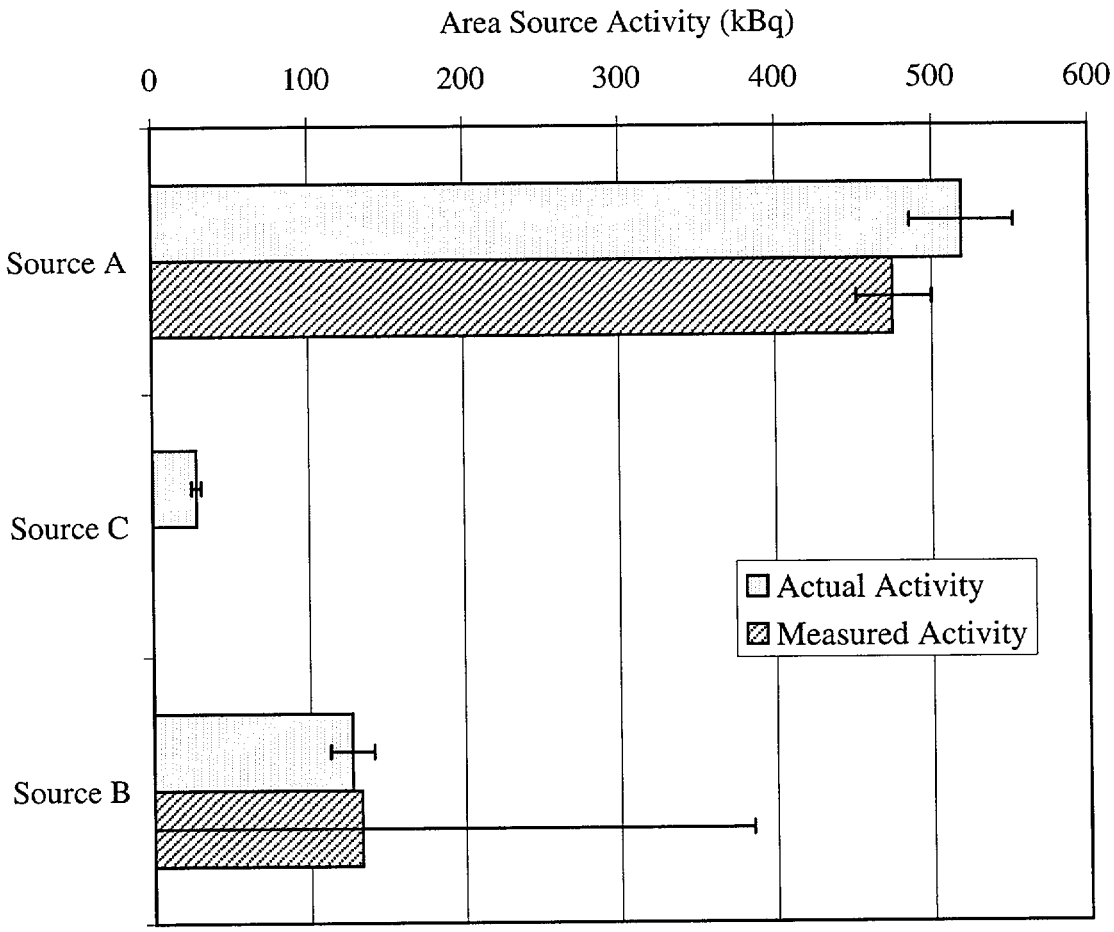
Area Source Activity (kBq)
0
100
200
300
400
500
600
Source A
Source C
Source B
Actual Activity
Measured Activity

Fig. 7(d).

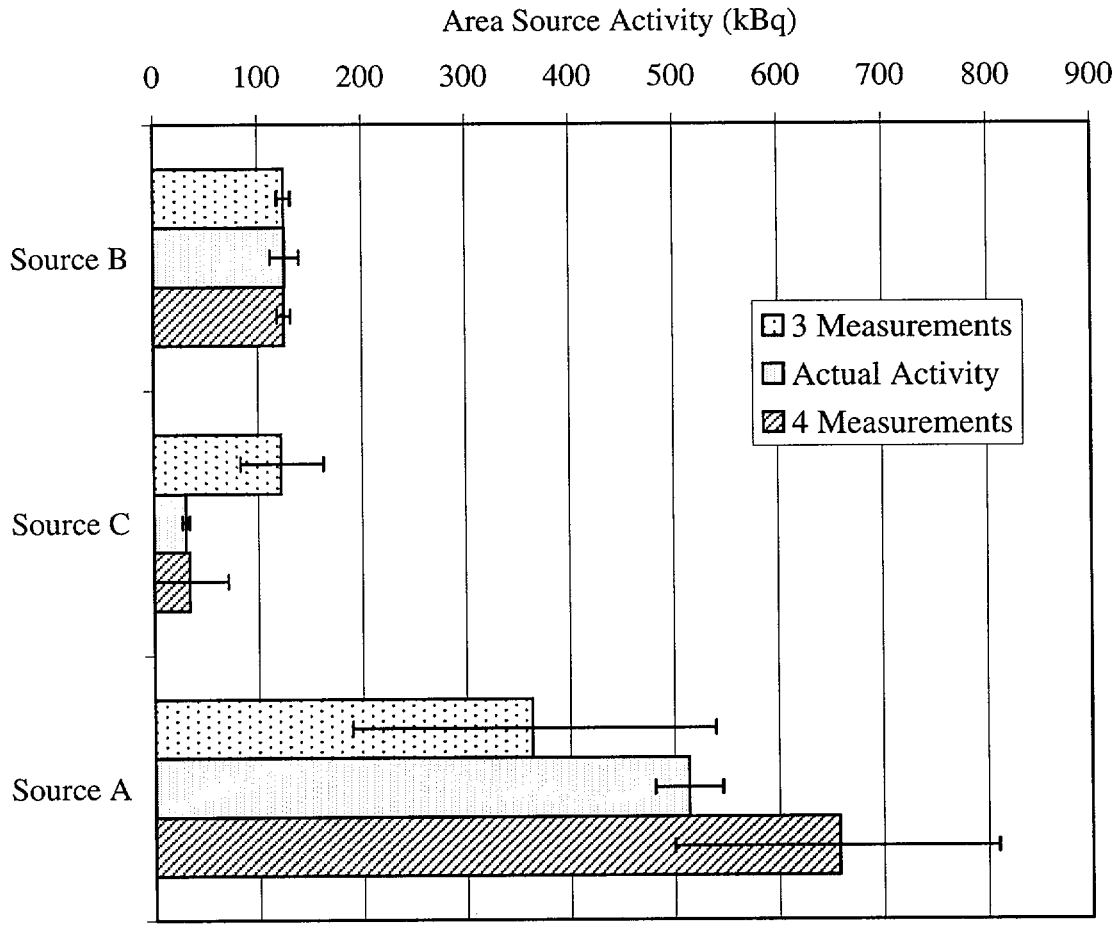
Area Source Activity (kBq)
0
100
200
300
400
500
600
700
800
900
Source B
Source C
Source A
3 Measurements
Actual Activity
4 Measurements

Fig. 8.

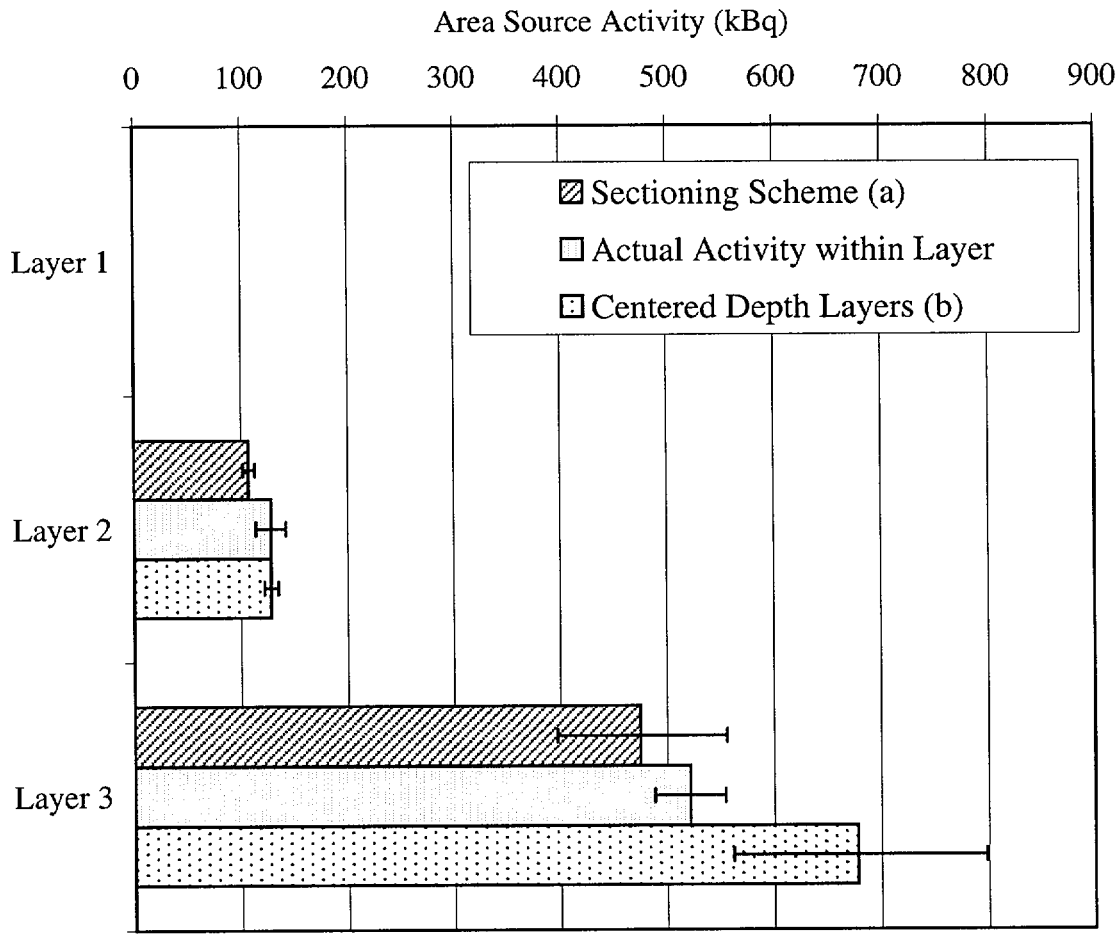
Area Source Activity (kBq)
0
100
200
300
400
500
600
700
800
900
Sectioning Scheme (a)
Actual Activity within Layer
Centered Depth Layers (b)
Layer 1
Layer 2
Layer 3

Fig. 9.

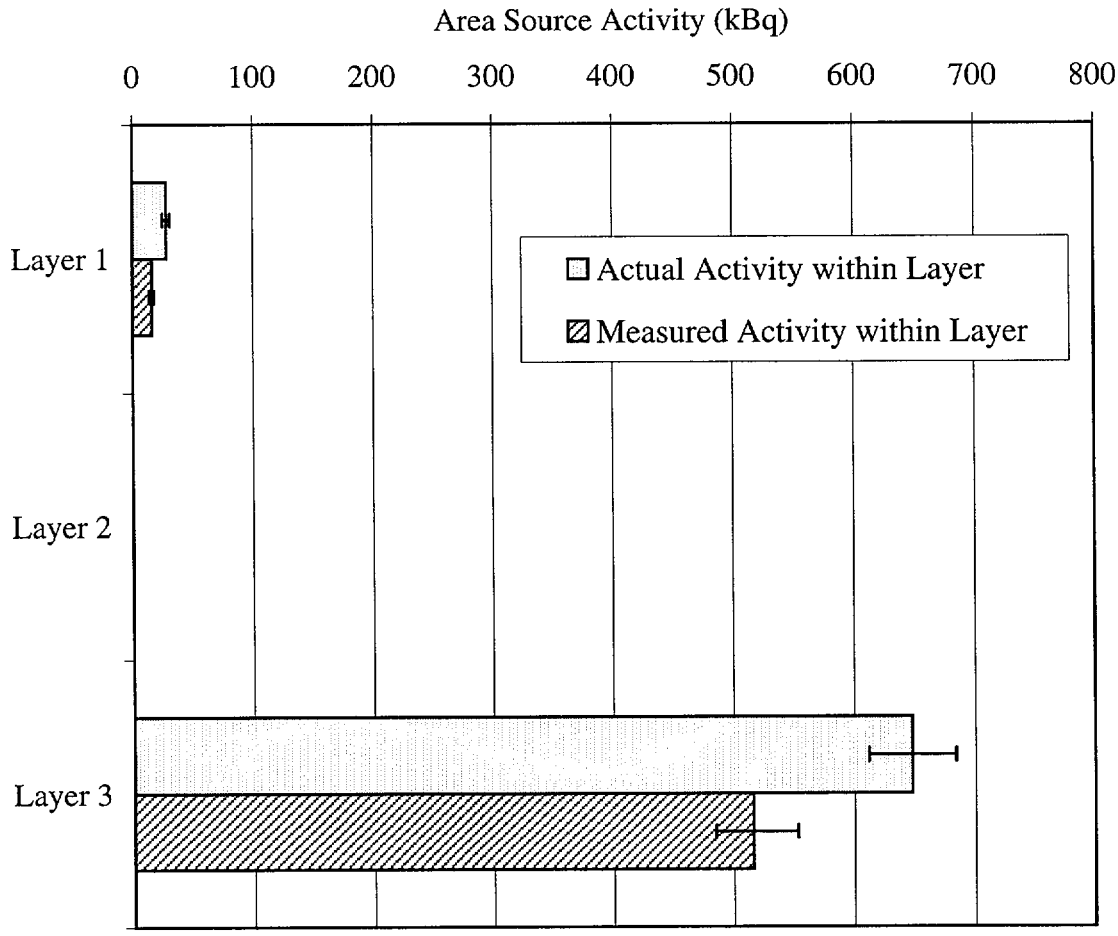
Area Source Activity (kBq)
0
100
200
300
400
500
600
700
800
Layer 1
Layer 2
Layer 3
Actual Activity within Layer
Measured Activity within Layer

Fig. 10.

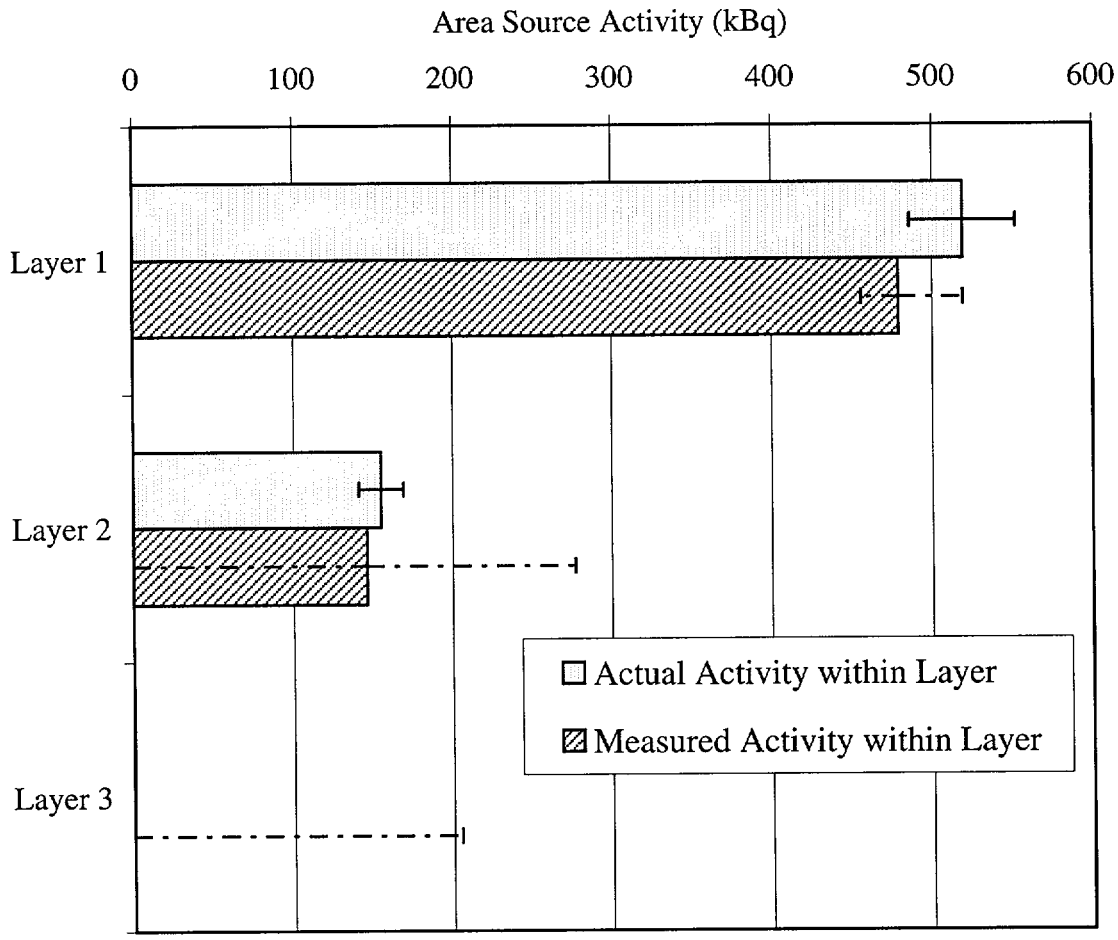
Area Source Activity (kBq)
0
100
200
300
400
500
600
Layer 1
Layer 2
Layer 3
Actual Activity within Layer
Measured Activity within Layer